Finescale Vertical Structure and Dynamics of Some Dryline Boundaries Observed in IHOP

QUN MIAO AND BART GEERTS

University of Wyoming, Laramie, Wyoming

(Manuscript received 9 August 2006, in final form 16 March 2007)

ABSTRACT

Several radar fine lines, all with a humidity contrast, were sampled in the central Great Plains during the 2002 International H_2O Project (IHOP). This study primarily uses aircraft and airborne millimeter-wave radar observations to dynamically interpret the presence and vertical structure of these fine lines as they formed within the well-developed convective boundary layer. In all cases the fine line represents a boundary layer convergence zone. This convergence sustains a sharp contrast in humidity, and usually in potential temperature, across the fine line. The key question addressed herein is whether, at the scale examined here (~10 km), the airmass contrast itself, in particular the horizontal density (virtual potential temperature) difference and resulting solenoidal circulation, is responsible for the sustained convergence and the radar fine line. For the 10 cases examined herein, the answer is affirmative.

1. Introduction

Clear-air weather radar surveillance scans often reveal "fine lines" during the warm season. These lines correspond with zones of sustained convergence and rising motion within the convective boundary layer (CBL) (Wilson et al. 1994; Geerts and Miao 2005). The CBL is best developed in the early afternoon and is populated with columns of rising, buoyant air ("thermals"; Stull 1988, p. 461). Thermals tend to penetrate higher in fine-line convergence zones, especially if the CBL is weakly capped (e.g., Karan and Knupp 2006; Sipprell and Geerts 2007, hereafter SG07). Therefore, under suitable conditions, thunderstorms are most likely to initiate along fine lines (e.g., Wilson and Schreiber 1986; Wilson et al. 1992; Wilson and Megenhardt 1997; Koch and Ray 1997). The organization and behavior of the ensuing deep convection may be strongly affected by the triggering fine line.

In late spring 2002, several fine lines were studied in detail as part of the International H_2O Project (IHOP), conducted in the central Great Plains, with the specific objective to improve understanding of convective initiation. While most of the fine lines initiating convection during IHOP were large-scale frontal boundaries or thunderstorm outflow boundaries (Wilson and Roberts 2006), most fine lines sampled by the IHOP armada (described in Weckwerth et al. 2004) were drylines, or at least carried a significant, sustained humidity gradient. Drylines commonly form in broadly convergent flow in west Texas, particularly in spring, and can occur under synoptically quiescent conditions (e.g., Schaefer 1974). Most of the IHOP dryline cases were observed farther north, and in synoptically active situations.

The objective of this study is to describe and dynamically interpret the meso-γ-scale (2–20 km) fine-line vertical structure and convergence. On the meso-β scale (20–200 km) or larger, drylines result from differential surface fluxes and the advection of distinct air masses. The convergence of these air masses is in part an isallobaric response to daytime pressure falls over west Texas (e.g., Crawford and Bluestein 1997; Bluestein and Crawford 1997), mainly due to the regional slope of the terrain, and a larger surface sensible heat flux on the drier west side. These mechanisms are well understood (e.g., Schaefer 1974; Sun and Ogura 1979; Sun and Wu 1992; Jones and Bannon 2002) and operate on a larger scale than examined here.

The scale over which structures and gradients are examined here is O(10 km), and the focus is on the cross-fine-line *vertical* circulation and associated thermodynamic contrast in the afternoon. The key question

Corresponding author address: Bart Geerts, Department of Atmospheric Sciences, University of Wyoming, Laramie, WY 82071. E-mail: geerts@uwyo.edu

DOI: 10.1175/2007MWR1982.1

to be answered is whether the density contrast in the CBL is responsible for meso-γ-scale convergence and fine-line formation. The null hypothesis is that the presence and strength of convergence lines is independent of the density contrast. This question can regard any radar fine line, but this study focuses on humidity boundaries, that is, drylines.

Much attention has been devoted to the finescale *horizontal* structure of several IHOP fine lines, especially the structure and evolution of misocyclones (Arnott et al. 2006; Markowski and Hannon 2006; Murphey et al. 2006; Xue and Martin 2006; Marquis et al. 2007). This along-line variability is not examined here, but we are aware that it modulates the flow, convergence, and vertical motion along the fine line, and thus may largely explain the difference between successive cross sections across the line.

The methodology is summarized in section 2. Two case studies are presented in section 3. Section 4 synthesizes and dynamically interprets findings from these case studies plus two Verification of the Origin of Rotation in Tornadoes Experiment (VORTEX) cases.

2. Methodology

a. Data sources and processing

This study primarily uses data collected aboard the University of Wyoming's King Air (WKA) aircraft. We examine data from 30–40-km-long transects across fine lines at elevations ranging between 150 and 1600 m above ground level (AGL), in particular the gust-probe winds along the flight track (roughly normal to the fine line) as well as water vapor mixing ratio (r) and potential temperature (θ). Water vapor is measured by a rapid-response Lyman-alpha probe, which was calibrated by a slow-response chilled-mirror dewpoint sensor.

The WKA carried the 95-GHz (W band) Wyoming Cloud Radar (WCR). The WCR simultaneously operated two fixed antennas, primarily in profiling (up/down) or vertical-plane dual-Doppler (VPDD) modes (Fig. 2 in Geerts et al. 2006). In the profiling mode, radar data portray the vertical structure of the CBL over its entire depth except for an ~220-m-deep blind zone centered at flight level. The VPDD mode allows an estimation of the along-track two-dimensional (2D) air circulation below the aircraft at a resolution of ~30 m. The extraction of the echo motion from the Doppler velocity measured from a moving platform, and the dual-Doppler synthesis, are discussed in Damiani and Haimov (2006).

Several other IHOP data sources were used. Low-elevation-angle reflectivity from various scanning ground-based radars were used to place the WCR transects in the context of radar fine lines. Data from both aircraft dropsondes and ground-based balloon sondes, collected in close proximity to the fine lines, were used to determine the CBL depth and airmass contrast.

b. Density-gradient-driven circulations

Radar fine lines are a manifestation of sustained linear convergence within the CBL (Wilson et al. 1994; Geerts and Miao 2005). The central hypothesis of this paper is that this convergence primarily results from a horizontal difference in buoyancy and thus in virtual potential temperature (θ_v). The horizontal scale of this convergence and θ_v difference ($\Delta\theta_v$) needs to be determined. Positive θ_v anomalies are buoyant; that is, they tend to rise spontaneously, at least if they are rather small scale (e.g., Houze 1993, p. 225; Doswell and Markowski 2004). Buoyant ascent implies a horizontal vorticity dipole (viewed in a vertical cross section) and roughly circular features (viewed on a map) with a diameter of O(1 km), depending on the CBL depth (e.g., Stull 1988, p. 461). These features should be present irrespective of the spatial organization of thermals, that is, whether or not the thermals are aligned by horizontal convective rolls (HCRs).

A horizontal θ_v gradient also drives a convergent solenoidal circulation that may lead to a density current, whereby the less dense air is forced over the denser air. In this case the buoyancy-induced horizontal vorticity is a single extreme, although under suitable ambient shear, a vorticity dipole may be present across the boundary (e.g., Rotunno et al. 1988). As will be illustrated below, such a singular extreme or dipole has a horizontal scale larger than that of thermals. Also, features tend to be elongated on a map since, to first order, the secondary circulation is 2D. The circulation produces a radar fine line, which separates the air masses of different density.

The slope of this fine-line echo, and of the associated updraft in a vertical plane, is evidence of wind shear ($\partial u/\partial z$), which can be large scale or local. If it is large scale, all echo/updraft plumes should be tilted. A tilted echo/updraft plume at the boundary only, surrounded by upright thermals, is evidence of local baroclinicity at that boundary. The Lagrangian change (D/Dt) of horizontal vorticity (η) due to baroclinicity can be estimated as

$$\frac{D\eta}{Dt} = \frac{g}{\theta_v}\frac{\partial \theta_v}{\partial x}, \tag{1}$$

where x is the boundary-normal direction [in the cases examined here, pointing (south)east], $\eta = (\partial u/\partial z) - (\partial w/\partial x)$,

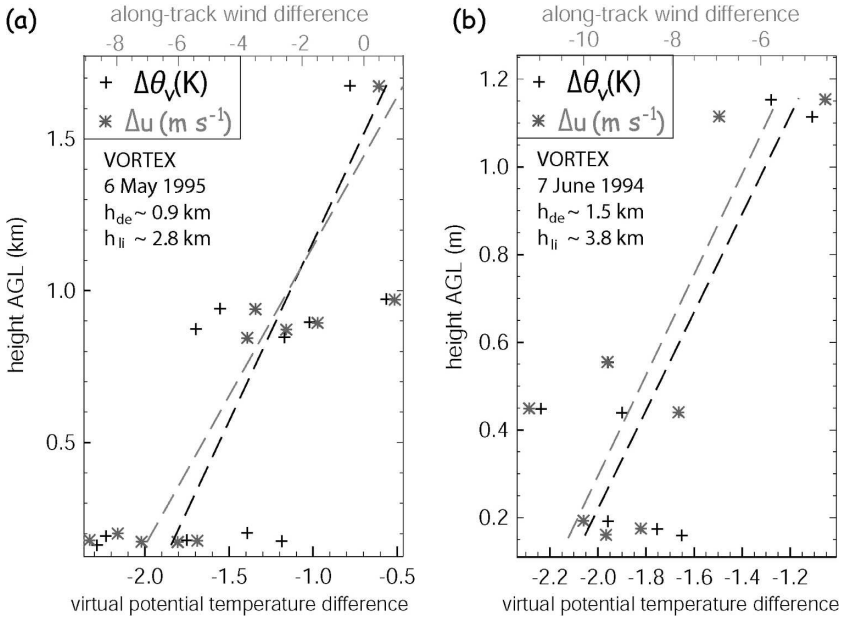

FIG. 1. Differences in along-track (approximately cross dryline) wind (gray symbols) and θ_v (black symbols) across two drylines documented during VORTEX, and best linear fit (dashed lines): (a) 6 May 1995 (Atkins et al. 1998; Ziegler and Rasmussen 1998); (b) 7 Jun 1994 (Ziegler and Rasmussen 1998). The differences are defined as moist ($x > 0$) minus dry ($x < 0$), and are computed from 10-km averages on either side of the dryline, for flight legs at various levels. The data were collected at 1-Hz frequency aboard the NOAA P-3 aircraft. The CBL depths listed are derived from Fig. 17 of Atkins et al. (1998) for (a) and Fig. 9 of Ziegler and Rasmussen (1998) for (b).

w is vertical velocity, and g is gravitational acceleration. In the cases examined below, the length scale is greater than the height scale (the depth of the CBL h) by a factor of 2 or more; thus, wind shear dominates η. In what follows we assume along-boundary uniformity ($\partial/\partial y = 0$). To start, we treat (1) as an initial value problem and examine the development of shear $(u_h - u_0)/h$ within an initially motionless CBL as a result of a steady gradient $\Delta\theta_v/\Delta x$, during a period Δt. Initially, advection by the baroclinically generated flow can be ignored. Thus (1) can be integrated vertically and in time to obtain

$$u_h - u_0 \cong \frac{g\Delta t}{\bar{\theta}_v} \int_0^h \frac{\Delta\theta_v}{\Delta x}\, dz,$$

where $\bar{\theta}_v$ is the average θ_v over $0 < z < h$. The $\Delta\theta_v$ driving this circulation is largest near the ground (where it is referred to as $\Delta\theta_{v,0}$) and decreases with height, as illustrated in Fig. 1 for two dryline cases described in the literature, and as confirmed in section 3a below.

The CBL depth h is defined as the level where potential temperature starts to increase with height. Experimentation has yielded the following objective criteria for sounding data: h is at the base of the layer where $(d\theta/dz) > [0.5\ \text{K}\ (200\ \text{m})^{-1}]$ and $(d\theta/dz) > [1.0\ \text{K}\ (1000\ \text{m})^{-1}]$, and nowhere within the 1000-m layer does θ decrease by over 0.2 K. The CBL depth on the denser side of the dryline (h_{de}) often is considerably less than the depth on the lighter side (h_{li}) (e.g., Fig. 17 in Atkins et al. 1998). In the two dryline cases shown in Fig. 1, h_{li} (on the dry side) was 2–3 times larger than h_{de}. Flight levels higher than that shown in Fig. 1 were not flown, but linear extrapolation of $\Delta\theta_v$ data shown in Fig. 1 suggests that $\Delta\theta_v$ nearly vanishes at h_{de}. The ratio of $\Delta\theta_v$ at h_{de} to $\Delta\theta_{v,0}$ is defined as R_θ, that is,

$$\Delta\theta_v \cong \Delta\theta_{v,0}\left[1 - (1 - R_\theta)\frac{z}{h_{\text{de}}}\right]. \tag{2}$$

For the cases shown in Fig. 1 and in section 3a, R_θ averages 0.37, ranging between 0.20 and 0.51. The above integral can be solved over $0 < z < h_{\text{de}}$ using (2), and the shear can then be estimated as

$$\frac{u_{h_{\text{de}}} - u_0}{h_{\text{de}}} \cong \frac{(1 + R_\theta)g\Delta t}{2\bar{\theta}_v}\frac{\Delta\theta_{v,0}}{\Delta x}. \tag{3}$$

This approximation is useful only in the initial stages (Δt small), before frictional dissipation and advection

become important. Later, an equilibrium develops, in which the *steady-state* secondary circulation (a form of kinetic energy) tries to destroy the horizontal $\Delta\theta_v$ (a form of potential energy) that is maintained by advection and/or surface heat fluxes. The convergence associated with this circulation can be estimated as follows, starting with (1):

$$\frac{g}{\theta_v}\frac{\partial\theta_v}{\partial x} = \frac{D\eta}{Dt} = u\frac{\partial^2 u}{\partial x\partial z} + w\frac{\partial^2 u}{\partial z^2}.$$

That is, the tendency term is ignored in the total derivative. The above relationship can be integrated over h_{de}:

$$\frac{g}{\bar{\theta}_v}\int_0^{h_{de}}\frac{\partial\theta_v}{\partial x}\,dz = \int_0^{h_{de}} u\frac{\partial^2 u}{\partial z\partial x}\,dz + \int_0^{h_{de}} w\frac{\partial^2 u}{\partial z^2}\,dz.$$

We now apply the chain rule twice, and assume 2D incompressible continuity $[(\partial u/\partial x) + (\partial w/\partial z) = 0]$ and $w = 0$ at $z = 0$ and $z = h_{de}$, to modify the right-hand side of the above equation as follows:

$$\begin{aligned}
&\int_0^{h_{de}} u\frac{\partial^2 u}{\partial z\partial x}\,dz + \int_0^{h_{de}} w\frac{\partial^2 u}{\partial z^2}\,dz \\
&\quad= \int_0^{h_{de}} u\frac{\partial^2 u}{\partial z\partial x}\,dz + w\frac{\partial u}{\partial z}\bigg|_0^{h_{de}} - \int_0^{h_{de}}\frac{\partial w}{\partial z}\frac{\partial u}{\partial z}\,dz \\
&\quad= \int_0^{h_{de}} u\frac{\partial^2 u}{\partial z\partial x}\,dz + \int_0^{h_{de}}\frac{\partial u}{\partial x}\frac{\partial u}{\partial z}\,dz \\
&\quad= \int_0^{h_{de}} u\frac{\partial^2 u}{\partial z\partial x}\,dz + u\frac{\partial u}{\partial x}\bigg|_0^{h_{de}} - \int_0^{h_{de}} u\frac{\partial^2 u}{\partial z\partial x}\,dz.
\end{aligned}$$

The first and third terms cancel. Thus,

$$\left(\frac{\partial u^2}{2\partial x}\right)_{h_{de}} - \left(\frac{\partial u^2}{2\partial x}\right)_0 = \frac{g}{\bar{\theta}_v}\int_0^{h_{de}}\frac{\partial\theta_v}{\partial x}\,dz. \tag{4}$$

Observations indicate that the boundary-normal confluence is strongest near the surface and, by extrapolation, vanishes near h_{de}. The average ratio of Δu at h_{de} to Δu_0, defined as R_u, is only 0.17 for the cases illustrated in Fig. 1 and section 3a. Thus, Δu vanishes at a slightly lower level than $\Delta\theta_v$. For simplicity we use the same linear expression (2) for the profiles of Δu and Δu^2, but with a slope R_u. Then a finite-difference expression of (4) becomes

$$-\Delta u_0^2(1 - R_u) \cong \frac{2\Delta x g}{\bar{\theta}_v}\int_0^{h_{de}}\frac{\partial\theta_v}{\partial x}\,dz$$

or

$$-\Delta u_0 \cong \frac{1}{1 - R_u}\frac{\Delta x g}{u_0\bar{\theta}_v}\int_0^{h_{de}}\frac{\partial\theta_v}{\partial x}\,dz. \tag{5}$$

In the absence of "ambient" flow, u_0 merely is the horizontal component of the solenoidal circulation. Using (2), (5) can be approximated as follows:

$$-\Delta u_0 \cong \frac{(1 + R_\theta)g h_{de}\Delta\theta_{v,0}}{2(1 - R_u)u_0\bar{\theta}_v}, \tag{6}$$

where the subscript "0" refers to measurements near the surface, in practice below $0.5h_{de}$. The magnitude of the confluence Δu_0 in (6) is affected by the rates of decline of $\Delta\theta_v$ and Δu with height in the CBL affect, and by u_0. In general, R_u should be close to zero, since diffluent return flow should occur in the upper CBL; however, the density contrast can be found over a greater depth. In practice, u_0 is calculated as the average low-level flow on the "dense" side of the boundary, minus the "ambient" flow (defined as the average low-level boundary-normal flow in nearby soundings on opposite sides of the boundary), and is positive toward the boundary. Note that u_0 is in the denominator of (6); when u_0 is small, as with some weak boundaries, its uncertainty can make confluence estimates based on (6) unreliable.

Expression (6) fundamentally is an application of the Bjerknes circulation theorem (Bjerknes 1898) and relates the steady-state low-level cross-boundary confluence ($-\Delta u_0$) to $\Delta\theta_{v,0}$ at corresponding horizontal scale. The term $-\Delta u_0$ is similar to convergence, but it does not imply a scale (Δu_0 is not divided by Δx), and the along-boundary component ($\partial v/\partial y$) is ignored. A similar expression has been obtained by Grossman et al. (2005), but they start from a circulation integral, and ignore the variation of $\Delta\theta_v$ with height.

Another relationship between confluence and density contrast can be obtained from density current theory. The boundaries examined herein may not have a sufficient $\Delta\theta_v$ to drive a classic atmospheric density current, as documented for instance for thunderstorm-generated gust fronts (e.g., Mueller and Carbone 1987) or cold fronts (e.g., Wakimoto and Bosart 2000); nevertheless, the theory may apply. Laboratory experiments suggest that the speed of a density current (U_{dc}) can be estimated as follows (Simpson and Britter 1980):

$$U_{dc} = K\sqrt{\frac{gD_{dc}\Delta\theta_v}{\theta_v}} + bU_{env}. \quad (7)$$

This equation is based on the horizontal momentum conservation equation (e.g., Houze 1993); U_{dc} bears similarity to the shallow water wave speed. Some form of (7) is commonly encountered in the literature, including in atmospheric applications. In (7) K corresponds with the Froude number; experimental values for K range from 0.7 to 1.0 or higher for atmospheric density currents (e.g., Wakimoto 1982; Mueller and Carbone 1987; Kingsmill and Crook 2003); U_{env} is the ambient low-level flow normal to and ahead of the density current. Laboratory work by Simpson and Britter (1980) indicates that $b = 0.70$. Numerical work by Liu and Moncrieff (1996) suggests that $b = 0.74$, ranging between 0.71 and 0.78. The density current depth (D_{dc}) is assumed to be equal to h_{de}, although this is uncertain (see section 4d below). The θ_v difference normally is measured on the ground; therefore $\Delta\theta_{v,0}$ is used in (7).

The movement of a boundary provides poor evidence for the density-current nature of the boundary (e.g., Smith and Reeder 1988). First, the estimation of the observed motion of the boundary is complicated by along-line variability. Second, the estimation of the theoretical boundary motion using (7) has several uncertainties, including the determination of the "ambient" low-level flow U_{env}. This determination is complicated by the ambient wind shear and variable CBL depth.

We can however measure the flow confluence ($-\Delta u$) with some accuracy, and it can be compared with the following estimate from density current theory. First, observations have shown that the feeder flow (U_{max}) exceeds the density current speed by about 40% (Simpson et al. 1977),

$$U_{max} \cong 1.40U_{dc}. \quad (8)$$

Thus the confluence normal to a density current, $-\Delta U_{dc}$, can be inferred from (7) and (8), assuming $K = 0.85$ and $b = 0.74$:

$$\begin{aligned} -\Delta U_{dc} &= U_{max} - U_{env} \\ &\cong 1.19\sqrt{\frac{gD_{dc}\Delta\theta_{v,0}}{\bar{\theta}_v}} + 0.04U_{env} \\ &\cong 1.19\sqrt{\frac{gh_{de}\Delta\theta_{v,0}}{\bar{\theta}_v}}. \end{aligned} \quad (9)$$

The neglect of the term $0.04U_{env}$ implies an uncertainty <1 m s^{-1}, which is less than other sources of error in this estimation. Both (6) and (9) relate the steady-state near-surface cross-boundary confluence to $\Delta\theta_{v,0}$ over the same horizontal scale. The main difference is that in the case of a solenoidal vortex (6), $|\Delta u| \propto h_{de}\Delta\theta_{v,0}$, while in the case of a density current (9), $|\Delta u| \propto \sqrt{h_{de}\Delta\theta_{v,0}}$.

Even though the term Δx does not appear in either (6) or (9), the horizontal scale over which these differences are computed clearly matters. The question of scale was raised by Atkins et al. (1998) and is further explored here. WKA wind and thermodynamic data are averaged over either $\Delta x = 3$ km or $\Delta x = 10$ km on either side of the leading edge of the boundary along all available low-level flight legs (below $0.5h_{de}$). The averaging is necessary in order to reveal small differences (the signal) embedded in much larger perturbations of convective origin (the noise). The choice of these scales is based on the following. A distance of 3 km should exceed the diameter of most coherent eddies (thermals) in the fair-weather CBL: aircraft data (e.g., Kaimal et al. 1976) and WCR vertical profile data (Miao et al. 2006) indicate that in the mid-CBL the diameter of most eddies is $1.5h$ or less. However HCRs generally have wavelengths longer than 3 km, and 10 km is about the maximum flight track distance generally (but not always) available on either side of the boundary in IHOP. The distance between the centers of the averaging domains on either side of the dryline equals the averaging distance Δx, because we do not assume a buffer zone around the boundary. The third and largest scale is the boundary-normal distance between soundings. In the cases examined here, this distance (Δx) ranges from 15 to 62 km. Sounding data differences are computed based on averages between the ground and $0.5h_{de}$.

The theory is tested first for a vigorous but shallow cold front observed on 24 May 2002 in west Texas (Xue and Martin 2006; Karan and Knupp 2006). This cold front had all the characteristics of a density current (Geerts et al. 2006): large $\Delta\theta_{v,0}$ values (3–6 K over scales of 3–19 km) and strong convergence ($-\Delta u$) at the head (8–11 m s^{-1} over the same scales) (Table 1). Both the solenoidal vortex Eq. (6) and the experimental density current Eq. (9) overestimate the low-level confluence at all scales, compared to observed values (Table 1).

3. Fine-line observations

Two case studies are presented below. Case studies of two other drylines in IHOP, on 24 May and 18 June 2002, can be found in Miao (2006).

a. 22 May dryline

On 22 May 2002 the IHOP armada studied a dryline fine line near the S-band dual-polarization Doppler ra-

TABLE 1. Analysis of the horizontal θ_v difference ($\Delta\theta_v$) and confluence ($-\Delta u$) for several fine-line boundaries, all with a humidity gradient, and comparison with theoretically estimated confluence values. The latter either assumes a steady solenoidal circulation [$-\Delta u_0$, see Eq. (6) in section 2b] or a density current [$-\Delta U_{dc}$, see Eq. (9)]. The factor R_θ and R_u in (6) are set at 0.37 and 0.17, respectively; these are averages for the profiles of $\Delta\theta_v$ and Δu on 22 May 2002, 6 May 1995, and 7 Jun 1994. The differences are scale dependent, and three different scales are assumed: flight-level WKA data are averaged over either 3 or 10 km on either side of the boundary (defined as the location of strongest humidity gradient), or the distance between two soundings on opposite sides of the boundary is used, if available. Only flight legs below $0.5h_{de}$ are used. Sounding data ("sonde") are averaged between the surface and $0.5h_{de}$. The distance between soundings is calculated normal to the boundary. Here u_0 is the mean boundary-normal flow on the dense side, minus the "ambient" low-level flow (positive toward the boundary).

Date	Boundary [dryline (DL)]	Source	Scale (km)	Δr (g kg^{-1})	$\Delta\theta_v$ (K)	h_{de} (m)	u_0 (m s^{-1})	Predicted $-\Delta u_0$ (m s^{-1})	Predicted $-\Delta U_{dc}$ (m s^{-1})	Observed $-\Delta u$ (m s^{-1})	Comments
22 May	Primary DL	WKA	3	2.7	−1.03	1600	5.8	7.3	8.4	4.0	Average of five flight legs between 2222 and 0009 UTC; see Fig. 6
		WKA	10	3.0	−1.33		6.0	9.1	9.6	4.7	Average of three flight legs between 2222 and 0009 UTC
	Secondary DL	WKA	3	1.4	−0.02		2.7	0.3	1.2	1.4	Average of the 2223 and 2355 UTC DL crossings; see Fig. 4
	Both DLs	Sonde	62	5.2	−4.46		7.7	23.8	17.5	8.9	See Fig. 1
24 May	Western DL	WKA	3	1.7	−0.29	1320	2.7	3.7	4.1	3.9	Average of two flight legs: one at 170 m AGL at 1948 UTC (see Fig. 9 of Weckwerth et al. 2004) and one at 400 m AGL at 1937 UTC (see Fig. 8 of Geerts et al. 2006)
		WKA	10	1.3	−0.24		4.5	1.8	3.7	3.3	Same as above, but second leg extends only 6 km into dry air
	Eastern DL	WKA	3	1.9	−0.46	1200	2.7	5.2	4.9	4.3	One flight leg at 200 m AGL at 2047 UTC
		WKA	10	2.2	−0.54		2.8	5.9	5.3	4.8	Same as above, but extending only 8 km into dry air
		Sonde	27	3.3	−0.72		4.2	5.3	6.4	4.9	Dry side: 2032 UTC Learjet dropsonde, 9 km west of the DL; moist side: 2035 UTC Learjet dropsonde, 18 km east of the DL
	Cold front	WKA	3	—	2.90	800	5.4	11.3	10.0	7.8	Same flight legs as for primary dryline; cold front moves at ~7 m s^{-1} to the southeast (Geerts et al. 2006)
		WKA	10	—	4.11		6.4	13.4	11.9	9.1	Same as above, but first leg only has 5 km in the cold air, and second leg only 6 km into the warm air
		Sonde	19	—	6.14		7.7	16.6	14.5	10.6	See Fig. 6 of Geerts et al. (2006)

TABLE 1. ⟨*Continued*⟩

Date	Boundary [dryline (DL)]	Source	Scale (km)	Δr (g kg^{-1})	$\Delta\theta_v$ (K)	h_{de} (m)	u_0 (m s^{-1})	Predicted $-\Delta u_0$ (m s^{-1})	Predicted $-\Delta U_{dc}$ (m s^{-1})	Observed $-\Delta u$ (m s^{-1})	Comments
18 Jun	Early phase	WKA	3	2.1	−0.35	1020	3.2	2.8	3.9	2.5	Average of seven flight legs below $0.5z_i$, between 1837 and 2138 UTC
		WKA	10	2.8	−0.84		3.7	5.9	6.1	3.0	Average of six flight legs below $0.5z_i$, between 1836 and 2115 UTC
		Sonde	32	3.1	−1.94		5.8	8.6	9.2	3.9	Dry side: 2022 UTC Mobile GPS/Loran Atmospheric Sounding System (M-GLASS) sounding, 11 km west of the DL; moist side: 2042 UTC M-GLASS sounding, 23 km east of the DL
	Late phase primary DL	WKA	3	2.4	−0.41	1500	6.4	2.4	5.1	1.7	Average of two flight legs below $0.5z_i$, between 2326 and 2341 UTC
		WKA	10	3.1	−0.87		7.6	4.3	7.5	2.2	Same as above
		Sonde	15	2.3	−1.05		7.1	5.6	8.2	3.0	Based on 2127 UTC (dry) and 2144 UTC (moist) M-GLASS soundings
	Late phase secondary DL	WKA	3	2.2	−0.19		4.0	1.8	3.5	5.5	Average of two flight legs below $0.5z_i$, between 2330 and 2337 UTC
		WKA	10	2.6	−0.46		4.7	3.7	5.4	5.7	Same as above
19 Jun	Early phase DL (dry side cooler)	WKA	3	1.2	0.32	1610	2.7	4.7	4.7	6.1	Based on two flight legs below 500 m AGL, both before 2000 UTC; see Fig. 12
		WKA	10	1.4	0.75		3.2	9.4	7.2	7.2	Same as above, but some leg length limits; see also Table 2 in SG07
		Sonde	18	2.0	0.59		3.6	6.6	6.4	7.7	See Fig. 7a
	Late phase DL (moist side cooler)	WKA	3	1.5	−0.49	1380	4.1	4.1	5.4	7.1	Based on two flight legs below 500 m AGL, after 2100 UTC
		WKA	10	2.9	−0.66		3.2	7.2	6.3	8.3	Same as above, but some leg length limits; see also Table 2 in SG07
		Sonde	38	3.8	−0.89		6.7	4.6	7.3	9.1	See Fig. 7b
7 Jun 1994	VORTEX DL	NOAA P-3	10	4.7	−1.9	1500	6.1	11.8	11.1	9.4	Six flight legs below 600 m AGL, between 2220 and 2348 UTC
6 May 1995	VORTEX DL	NOAA P-3	10	5.7	−1.8	1300	7.0	8.8	8.2	7.0	Five flight legs at ~180 m AGL, between 2146 and 2358 UTC

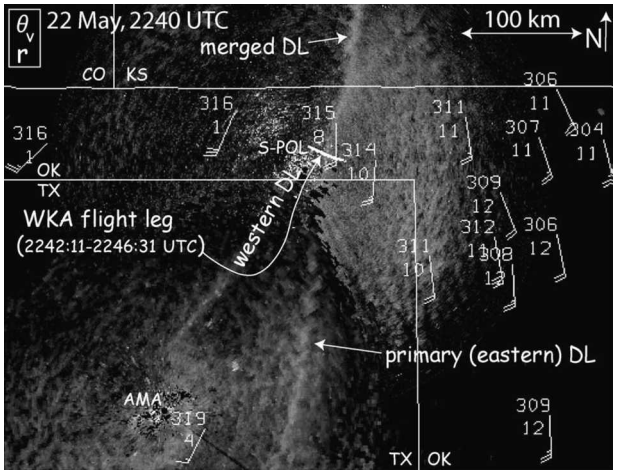

FIG. 2. Radar reflectivity and surface station observations near the dryline (DL) on 22 May 2002. The reflectivity field, ranging from −5 (black) to +30 dBZ (white), is from the 0.5° scans of the Amarillo, TX (AMA), WSR-88D and S-Pol radars. Here θ_v (K) and r (g kg^{-1}) are plotted instead of the conventional temperature and dewpoint. A full barb is 5 m s^{-1}. The time shown in the upper left applies to the station data. Radar data were collected within a few minutes of this time.

dar (S-Pol) in the Oklahoma Panhandle. Two fine lines developed: a more defined one to the east (the "primary dryline") and a less apparent line to the west (Fig. 2; Fig. 3 in Weiss et al. 2006). These lines merged north of the IHOP operations. The humidity and temperature contrasts between the moist and dry air masses were considerable (Fig. 3; as well as Fig. 4 in Demoz et al. 2006); the air mass between the two drylines had intermediate properties. The soundings shown in Fig. 3 indicate that the moist-air θ_v was 4.5 K lower than that on the dry side (Table 1). Even larger θ_v differences across the dryline complex existed at the surface (Fig. 2). The dry-side CBL was remarkably deep, and about twice as deep as the moist-side CBL depth (h_{de}), which is too deep for the CBL depth to be inferable from WCR profiles (Miao et al. 2006); the temperature of the upper ~1 km of this CBL was below the threshold of most insects. But east of the eastern dryline, WCR-inferred CBL heights corresponded well with the thermodynamic CBL height (Fig. 4).

Clear-air reflectivity imagery, for instance from S-Pol, indicates that the convergence zone of the primary dryline had a sharply defined western edge and a more fuzzy eastern edge (Fig. 2; top panels of Fig. 2 in Demoz et al. 2006; Fig. 4a in Weiss et al. 2006). This contrast is most apparent at greater radar range, where S-Pol sampled the upper CBL. That suggests that lofted insects were carried eastward over moist-air wedge. In other words, westerly shear across the dryline (Fig. 3) tilted the dryline updraft eastward and caused an eastward trailing echo anvil.

This eastward tilt of both fine lines is apparent in transects of WCR reflectivity, for instance at 2220 and 2243 UTC (Fig. 4). The echo anvil is most obvious east of the eastern dryline at 2243 UTC (Fig. 4h). The air

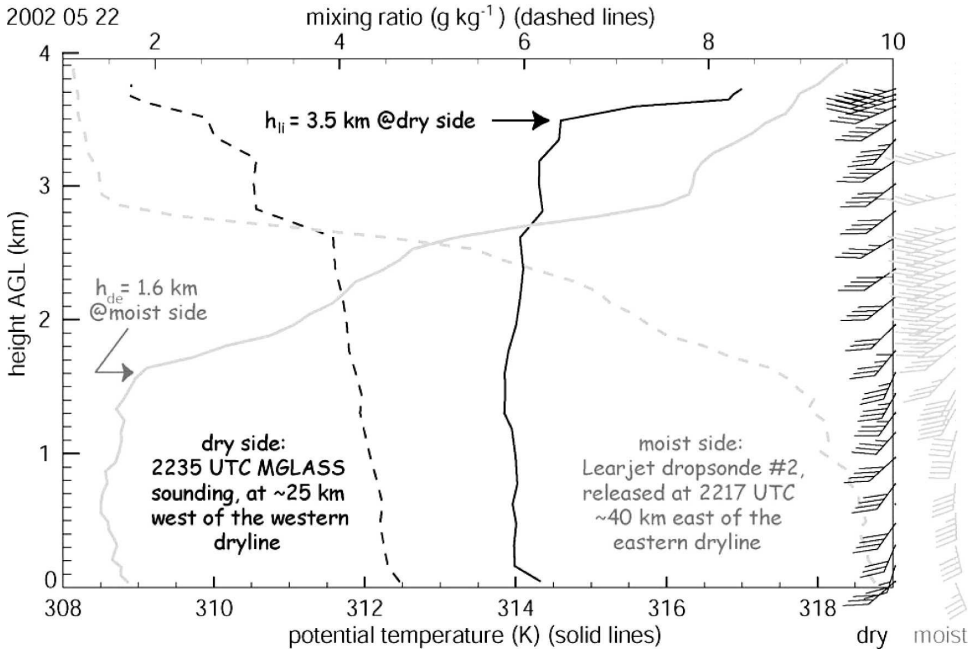

FIG. 3. Profiles of r and θ derived from two near-simultaneous soundings released on opposite sides of the 22 May 2002 split dryline. Gray (black) lines and symbols refer to the moist (dry) side.

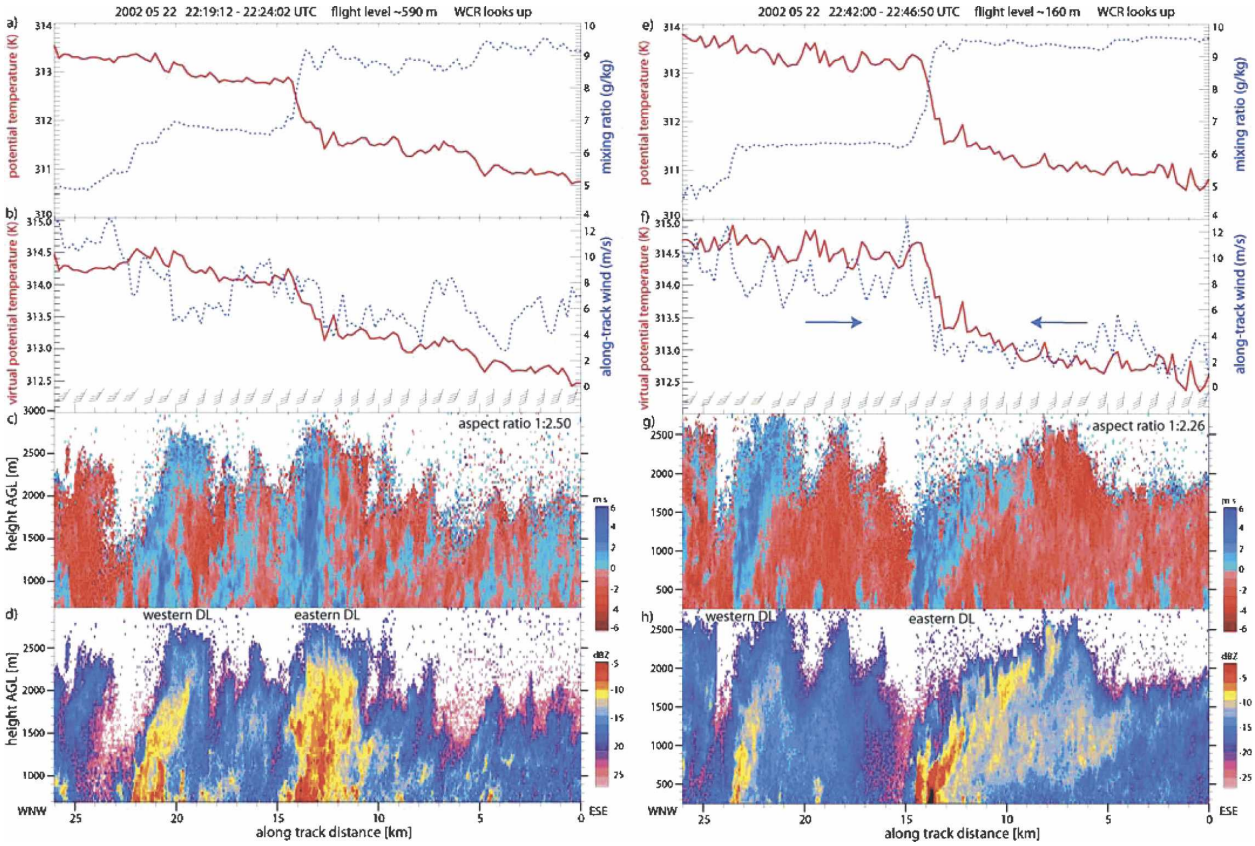

FIG. 4. WKA observations of the 22 May dryline (DL) system, along two transects, on the left around 2220 UTC (flight level ~590 m AGL), and on the right around 2243 UTC (flight level ~160 m AGL). The horizontal axis is distance along the flight track; the reference point ($x = 0$) is arbitrary but is the same in both transects. In this and other transects, the moist side is on the right. (a), (b), (e), (f) Flight-level data are shown on top. This includes the along-track (dryline normal) wind and the horizontal wind barbs (full barb = 5 m s^{-1}). Along-track flow convergence occurs when the blue trace descends from left to right in (b) and (f), and the main convergence belt is highlighted by the opposing blue arrows. (c), (g) WCR vertical velocity (positive values indicate ascent), and (d) and (h) corresponding WCR reflectivity in the vertical plane above the aircraft. In the WCR plots the vertical axis (height) is exaggerated somewhat (see "aspect ratio"); this makes the tilt of plumes less apparent.

was moister and cooler on the east side of both lines, but the eastern line, with higher reflectivity values, had a larger temperature and humidity contrast, as well as more convergent flow. The latter is evident from the gust probe wind normal to the dryline (Figs. 4b,f), and from the WCR vertical velocity field (Figs. 4c,g). The flight-level along-track confluence resulted from slight changes in the direction of a strong wind, mainly across the eastern dryline (see wind barbs in Figs. 4b,f): the wind in the CBL generally blew at ~20 m s^{-1} from the south-southwest, along the dryline, but east of the dryline it was more southerly and stronger. The eastern line was especially marked by strong updrafts, up to ~5 m s^{-1}. The dryline echoes penetrated well above h_{de} (Figs. 4d,h; Fig. 9 in Weiss et al. 2008), notwithstanding the low temperature near the echo tops (12°C at 2700 m AGL).

The θ_v gradient across the primary dryline is about 1.0 K over 3 km, and 1.3 K over 10 km (Table 1). No measurable local θ_v gradient exists across the secondary western dryline. (Only 3-km averages are available for this boundary.) The 10-km $\Delta\theta_v$ across the primary dryline is only 30% of the $\Delta\theta_v$ across 62 km (Table 1), implying a broader (meso-β) θ_v gradient.

The updraft tilt is consistent with the θ_v gradient across the primary dryline; that is, it appears to be due to baroclinically generated horizontal vorticity. The weak θ_v gradient across the western dryline may explain why this line gradually disappeared, mostly between 2220 and 2320 UTC (e.g., Fig. 2 in Demoz et al. 2006).

A cross-dryline circulation was well established at 2326 UTC (Fig. 5). A 6.7 m s^{-1} strong rear-to-front current (highlighted in the red box in Fig. 5b) advected low-θ_v air toward the leading edge, which was tilted about 45° from vertical. Because the primary dryline was quasi stationary at this time, the flow shown in Fig.

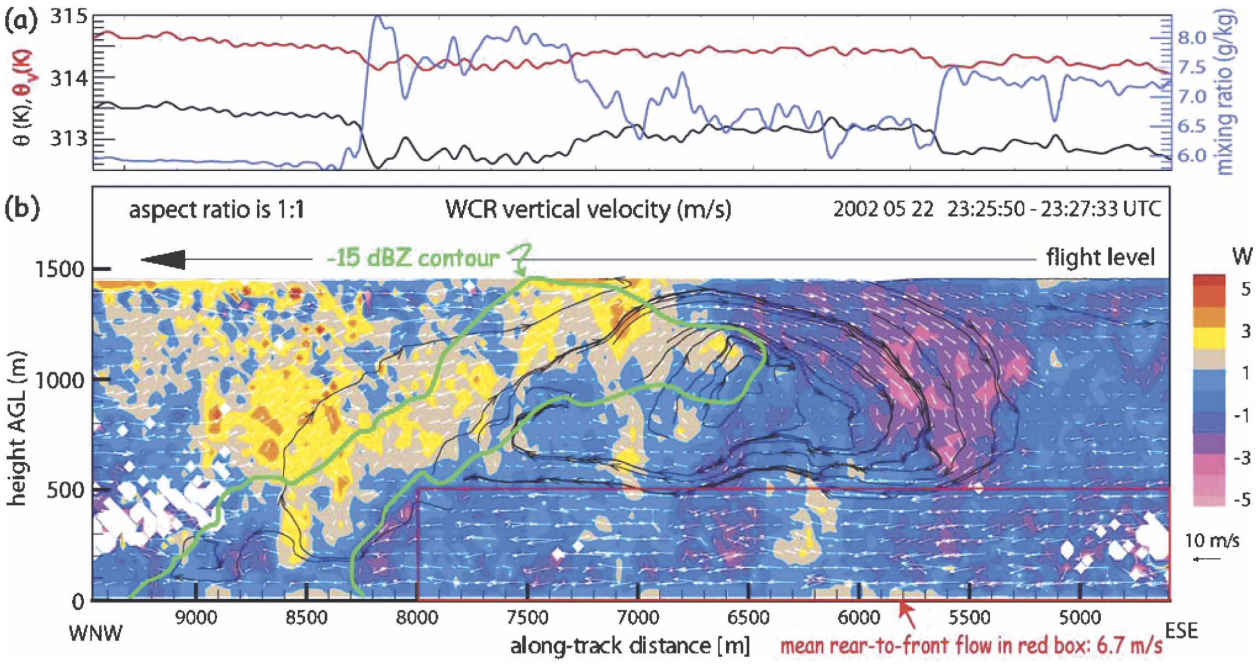

FIG. 5. (a) WKA flight-level data and (b) WCR vertical-plane dual-Doppler wind field across the 22 May primary dryline around 2326 UTC. The vector field is visually enhanced by objectively drawn streamlines (black lines with arrows). The vertical velocity field is shown in color. The nadir antenna −15-dBZ contour, enclosing the strongest echoes, is shown in green.

5b can be thought of as relative to the boundary, which resembled a density current head. At flight level (~1540 m AGL) this head was intercepted between $7300 < x < 8200$ m (Fig. 5b); air in this region had r and θ values between those characterizing the dry and the moist air masses at lower levels (Fig. 4e). This confirms observations by Ziegler and Hane (1993) that the head is a mixing zone. One mixing mechanism must be the recirculation of flow into the head: to the rear of the head, a strong downdraft mixes air into the rear-to-front current (Fig. 5b). At the time of the WKA crossing, the air in the head was generally rising but negatively buoyant (Fig. 5a). This negative buoyancy and the strong downdraft behind the head are additional indications of density current dynamics.

Farther east of the primary dryline the moist air was sampled intermittently at flight level (not shown), which roughly corresponds with h_{de} (Figs. 4d,h; Fig. 1). Thus the CBL top had undulations, possible trapped lee waves behind the density current head (e.g., Weckwerth and Wakimoto 1992; Jin et al. 1996). The WCR reflectivity profiles reveal no evidence of breaking Kelvin–Helmholtz (KH) waves. Such waves were observed in the case of the 24 May cold-frontal density current, marked by a thrice-stronger θ_v gradient over 10 km (Table 1). In that case the minimum value of the Richardson number (Ri) at the interface between denser and lighter air was ~0.1 (Geerts et al. 2006). The moist-side temperature and wind profiles on 22 May (from the sounding shown in Fig. 1), filtered to a vertical resolution of 100 m (as done in Geerts et al. 2006), yield a minimum Ri of 0.4 just above h_{de}. KH instability occurs when Ri < 0.25 (e.g., Miles and Howard 1964; Mueller and Carbone 1987). Thus the θ_v deficit of the 22 May dryline density current appears insufficient, or rather the resulting shear at the interface is too weak, to generate breaking KH waves.

The horizontal vorticity within the ~1-km-diameter solenoid highlighted by black streamlines in Fig. 5b is about 2×10^{-2} s^{-1}. An earlier VPDD transect, at 2201 UTC (1.4 h earlier), showed no coherent circulation across the dryline; at that time the dryline plume was essentially upright. Flight-level data from the primary-dryline crossings below $0.5h_{de}$ show a steady increase of $\Delta\theta_v$ over 3 km from 0.69 to 1.31 K between 2222 and 2356 UTC. The mean θ_v gradient [1.03 K (3 km)$^{-1}$; Table 1] can produce the observed horizontal vorticity in 0.75 h, according to (3). Thus the circulation at 2326 UTC (Fig. 5b) could have been generated in the time available and may have become rather steady. Even during the short time period between 2220 and 2243 UTC an increase in echo tilt of the primary dryline is apparent (Figs. 4d,h) and, correspondingly, an increase in θ_v gradient and in confluence. (It is possible that this difference between the two transects in Fig. 4 is not a uniform temporal change but is rather due to along-line

variability advecting into the geographically fixed track from the south.) Between 2300 and 0000 UTC, the primary dryline began to retrograde (move westward), at a speed of 2–3 m s^{-1} by 0000 UTC.

Vertical variations of the airmass difference across the 22 May primary dryline are shown in Fig. 6. In all transects the moist air mass is sufficiently cooler, such that it is also denser. Both Δr and $\Delta\theta_v$ decrease with height, as do the VORTEX drylines (Fig. 1), but the level where the extrapolated Δr and $\Delta\theta_v$ values reach zero is lower, only slightly above h_{de}. The flow is convergent in all transects except one[1] (Fig. 6c), and Δu also tends to be strongest at low levels. The dry air rises relative to the moist air in most transects, especially at low and middle levels (Fig. 6c). The slopes of $\Delta\theta_v$ and Δu are used in the estimation of R_θ and R_u [Eq. (6); Table 1].

The dryline convergence zone (DCZ) can be several kilometers wide yet the term humidity "discontinuity" is appropriate at the scale of the coherent eddies captured by the WCR. The rapid change in r is evident in Figs. 4a,e, and the horizontal gradient $\Delta r/\Delta x$ averaged over 300 m (Fig. 6d) across the dryline is almost 10 times as large as that averaged over 3 km (Fig. 6a), and nearly the entire humidity change is concentrated in 300 m. Yet the θ_v change is less discontinuous: $\Delta\theta_v/\Delta x$ over 300 m (Fig. 6d) is only 3 times larger than that over 3 km (Fig. 6b). The presence of a humidity jump sharper than the θ_v change generally applies to the other IHOP cases studied here; data for the two VORTEX cases shown in Fig. 1 do not allow this finescale comparison.

The observed cross-dryline confluence ($-\Delta u_0$) is compared to the one expected assuming a steady-state solenoidal circulation (6) and a density current (9) (section 2b) in Table 1. Both theoretical estimates are high (as for the 24 May cold front), and far higher than observed at a length scale of 62 km, indicating that (6) and (9) do not apply at a larger scale in the presence of a large-scale θ_v gradient. This agrees with the dryline study of Atkins et al. (1998): they find that density current theory can be applied at 5 km, but not at 50 km.

In summary, the moist air mass just east of the 22 May primary dryline developed a θ_v deficit of sufficient magnitude to drive solenoidal circulation with sloping updraft and an echo plume trailing toward the moist air. WCR transects and flight-level data support the notion of a density current, with a well-defined leading head and low-level rear-to-front flow. Density current characteristics are evident in all WKA/WCR transects except the earliest one, notwithstanding significant along-line variability and an along-line flow far stronger than the solenoidal circulation.

b. 19 June dryline

On 19 June 2002 the IHOP armada examined a synoptic-scale frontal shear zone in northwest Kansas (Murphey et al. 2006; SG07). Weak southwesterly flow converged at a prefrontal dryline with a southerly low-level jet confined in the moist air mass (Fig. 7). Deep convection erupted along the dryline near 2130 UTC, in particular in the vicinity of misocyclones that modulated the moisture and vertical velocity field (Murphey et al. 2006; Marquis et al. 2007). These misocyclones resulted from strong horizontal wind shear across the dryline, far stronger than on 22 May. This is evident by comparing the flight-level wind barbs in Fig. 4 to those in Fig. 8. SG07 have shown that the dryline updraft and echo plume tilted toward the west in an early phase, when the dryline progressed eastward, and later their slope reversed, toward the moist side, while the dryline became quasi stationary. The change in slope of the updraft was accompanied by a circulation reversal. Soundings were collected on both sides of the dryline, in relative proximity to the dryline, both in the early and later phases (Fig. 7). Initially θ_v was slightly lower on the dry side, which is unlike any dryline reported on in this study, but has been recorded before (Fig. 4 in Crawford and Bluestein 1997). In the course of ~1.5 h, between 1330 and 1500 local solar time, the CBL warmed and deepened on the dry side, resulting in a lower mixing ratio, due to the entrainment of dry free-tropospheric air into the deeper CBL. Yet on the moist side the stable layer above the CBL subsided, and the CBL temperature and humidity changed little. As a result, the humidity and mainly temperature contrasts across the dryline increased, and the net effect was that air on the moist side became denser.

In both phases the updraft and echo slopes are dynamically consistent with the observed buoyancy gradient across the dryline: in the early phase air on the dry side is denser (Fig. 8a), but as the dry side warms faster than the moist side, the θ_v gradient has a reversed sign in the late phase (Fig. 8d). The transition from a westward-tilted boundary, with denser air on the dry side, to an eastward-tilted dryline with denser air on the moist side is examined further in Fig. 9, using WKA data within the CBL. Some drying occurs during the early afternoon, but the humidity difference persists. Thus

[1] The one exception (at 2201 UTC, at a flight level of 1470 m) could be discounted because, even though there is a small humidity difference (0.6 g kg^{-1}), the CBL is shallower at this time, the $\Delta\theta_v$ values are insignificant, both at flight level (0.23 K) and on the ground (<0.5 K), and the density current circulation is not yet present, as mentioned above.

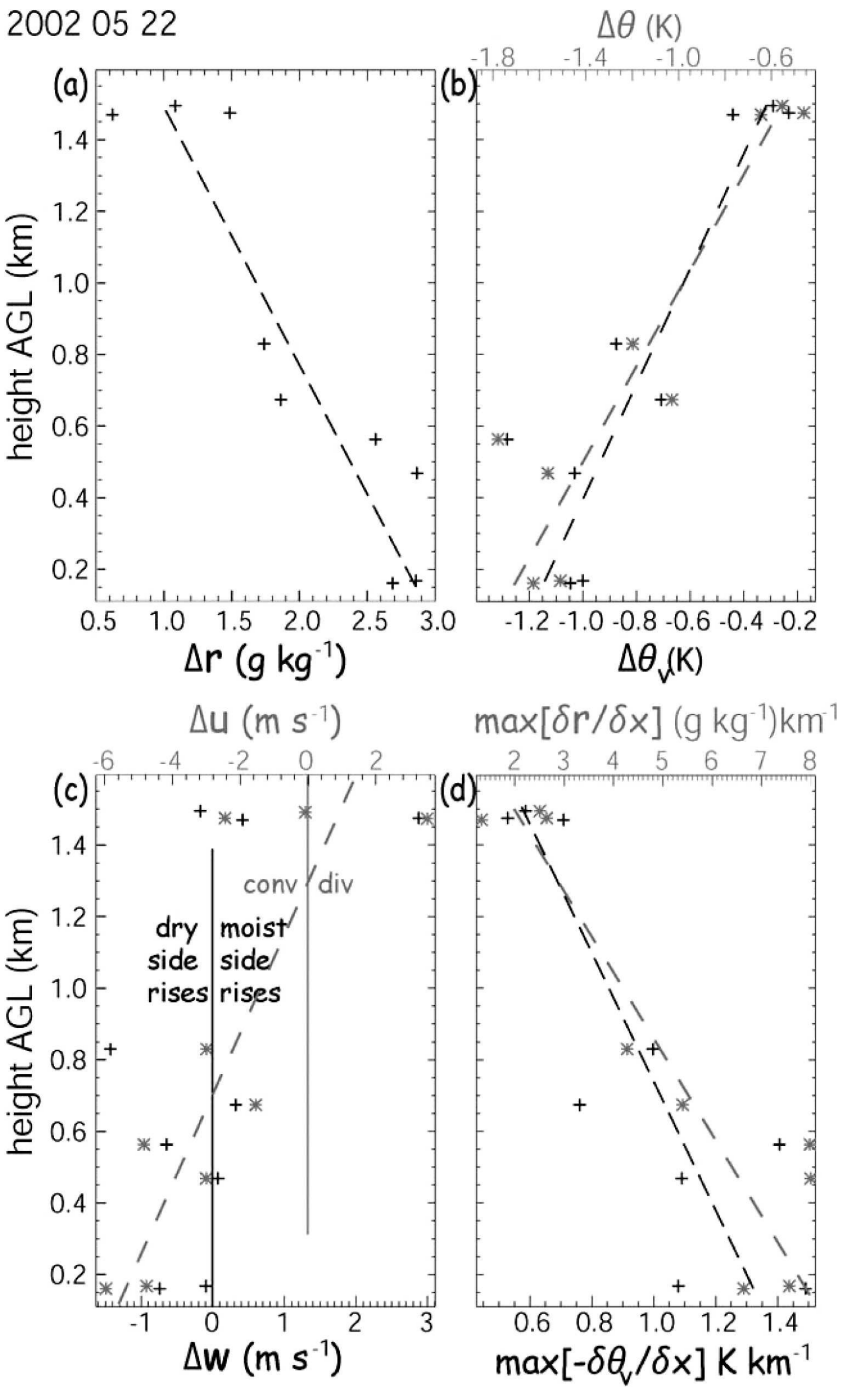

FIG. 6. Profiles of the difference between moist and dry air on 22 May, based on in situ WKA data at various flight levels between 2207 and 2350 UTC. The difference (moist − dry) is based on 3-km averages, on opposite sides of the primary dryline, which was marked by a clear humidity gradient. The top of the vertical axis is $h_{de} \cong 1.6$ km (Fig. 3). Black plus symbols refer to the lower axis and gray stars to the upper axis. The dryline-normal wind (u) and vertical air motion (w), shown in (c), are obtained from the gust probe. In (d) the maximum gradient at the dryline is shown, over $\delta x = 300$ m, for 100-m filtered values. Dashed lines indicate linear best fits.

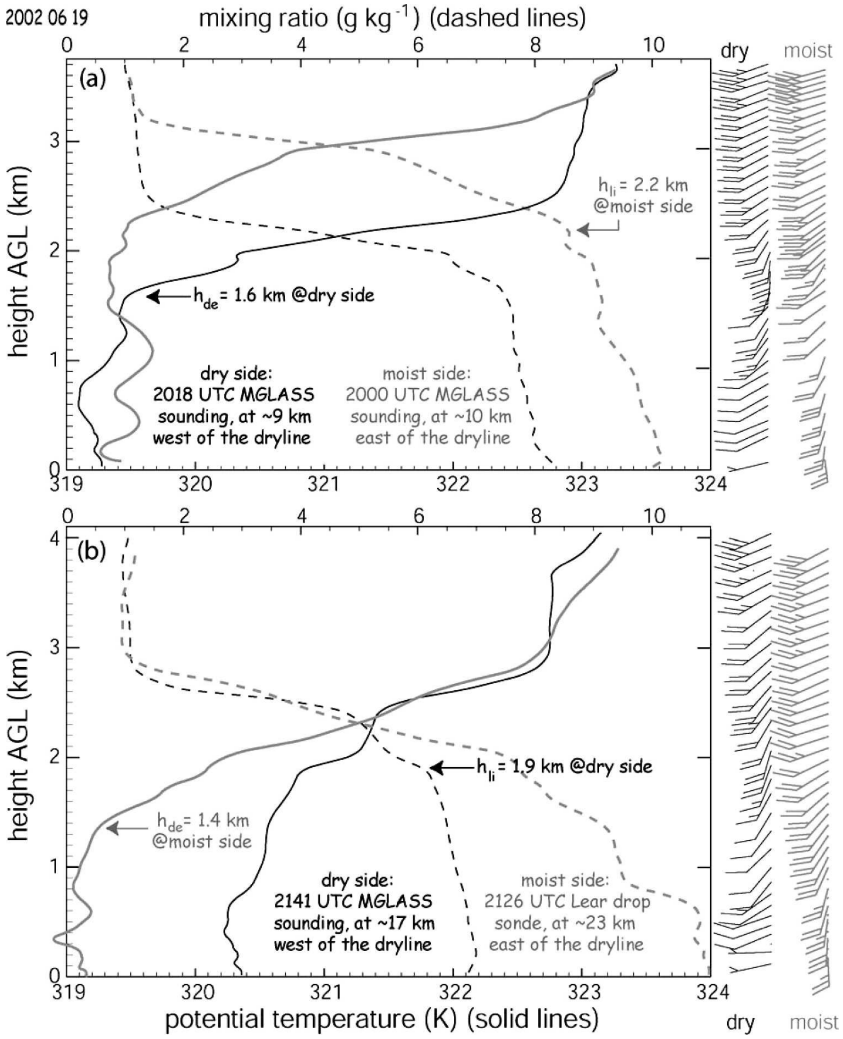

FIG. 7. As in Fig. 3, but for the 19 Jun 2002 dryline: (a) early phase (θ_v higher on the moist side); (b) late phase, nearly 1.5 h later (θ_v higher on the dry side). Note the correspondence of the x axes in (a) and (b).

the reversal of the θ_v gradient is entirely due to differential warming: the dry-side CBL warms more than the moist-side CBL, due to advection and/or surface sensible heat flux. The $\Delta\theta_v$ is small both in the early and the late phases, less than 0.5 K at the 3-km scale (Table 1), and less than 1.0 K at the 10-km scale and according to the sounding pairs. So the resulting solenoidal circulation should be weak.

Indeed, weak solenoidal circulations, weaker than the one observed on 22 May (Fig. 5b) have been documented in both phases (SG07), although an updraft/downdraft dipole is not always apparent (e.g., Fig. 8e). Indirect evidence for the secondary circulation and its reversal arises from the WCR reflectivity profile across the dryline. The higher reflectivity on the moist (denser) side of the 22 May primary dryline (Figs. 2, 4h) was interpreted as the result of a solenoidal circulation. In the early traverses the WCR reflectivity peaks near the humidity jump that marks the dryline and continues to be high to the west (Fig. 9d), suggesting a solenoidal circulation with upper-CBL transport to the west; during the last two traverses the lowest reflectivity values are found to the west, and higher values are found near and to the east of the dryline. The WCR vertical velocity pattern is consistent with this (Fig. 9e): in the early (late) phase rising motion tends to occur just east (west) of the dryline; however, this signal difficult to discern in a vigorously convective BL.

Low-level WKA dryline traverses indicate that the confluence is 6–7 m s^{-1} over 3 km for both phases (Table 1). This is stronger than what can be expected from baroclinicity at this scale (6–7 m s^{-1}). This applies

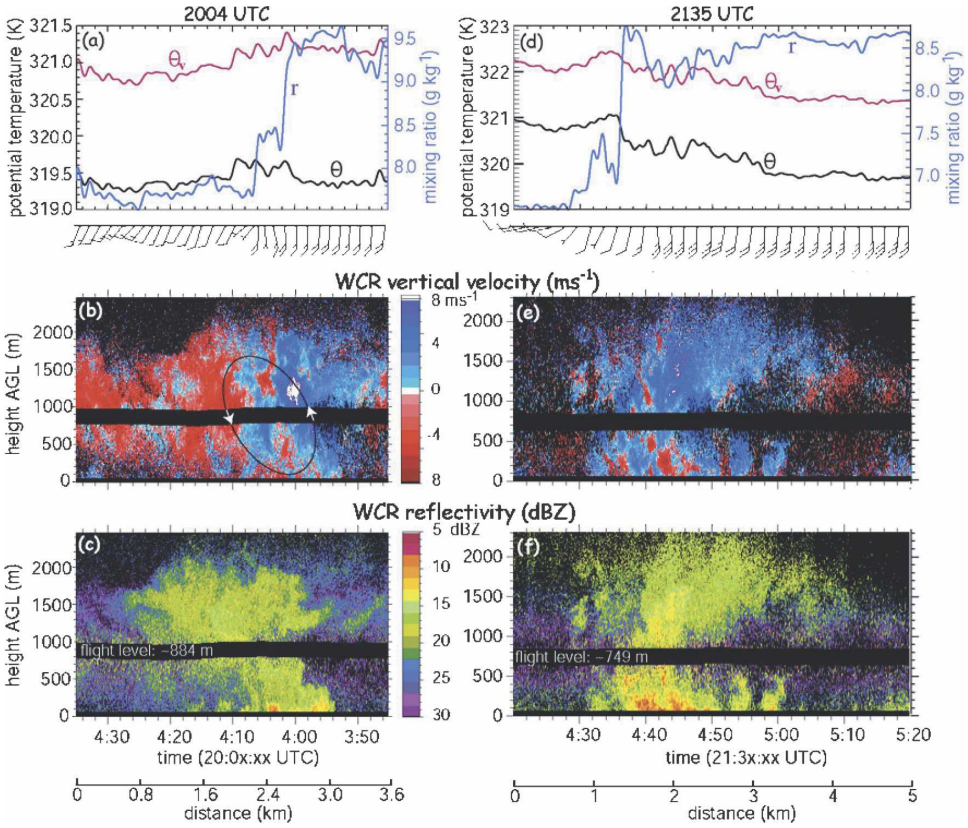

FIG. 8. Flight-level data and WCR vertical transects above and below flight level for the 19 Jun 2002 dryline, during the (a)–(c) early phase (2004 UTC) and (d)–(f) late phase, 1.5 h later. The flight-level gust probe wind is shown as barbs above the WCR vertical velocity panel. The direction of the solenoidal circulation is shown in (b).

at other scales as well (except for the 10-km scale in the early phase; Table 1). It is remarkable that it applies even to the largest scale: the Δu between the two late-phase soundings, 38 km apart, is above the two theoretical Δu estimates. As mentioned before (section 3a), the density current confluence at such scale tends to be an overestimate in the presence of a background θ_v gradient.

Thus some other mechanism may have contributed to finescale convergence leading to the 19 June dryline fine line. Additional evidence for this arises from the fact that at some time between the two phases illustrated in Fig. 8, $\Delta\theta_v$ must have been zero for the reversal to occur. Yet throughout the period, Doppler-on-Wheels (DOW)-3 reflectivity and velocity data indicate that the dryline remained well defined and that the cross-dryline flow was convergent. Horizontal-plane WCR velocity data for an along-dryline flight leg at 2040–2047 UTC indicate strong convergence at <1-km scale (Fig. 11 in SG07).

It is not clear what mechanism explains the rather strong finescale convergence during all phases of the 19 June dryline. One possibility is that it was driven by buoyancy relative to both adjacent air masses. Such buoyancy, with a θ_v' magnitude of ~1 K, was evident from a dropsonde transect (Fig. 13b in SG07) and, on a smaller scale, from a stepped WKA traverse (Fig. 12a in SG07), both just prior to CI. It is evident also on a scale of a few kilometers, although the magnitude is only ~0.5 K at 2135 UTC (Fig. 8d). This buoyancy may explain why mainly ascending motion occurs at this time, rather than a solenoidal circulation (Fig. 8e). The flight-level wind field (shown below Fig. 8d) suggests strong vertical vorticity near the dryline between $1.2 < x < 2.0$ km, roughly collocated with the main updraft in the WCR transect. At this time the WKA intersected an intensifying misocyclone, labeled "J" in Fig. 6 of Marquis et al. (2007).

A second possibility is downward transfer of momentum toward the dryline, on either side of the dryline, although evidence presented in section 4b argues against that process. Third, larger-scale dynamics con-

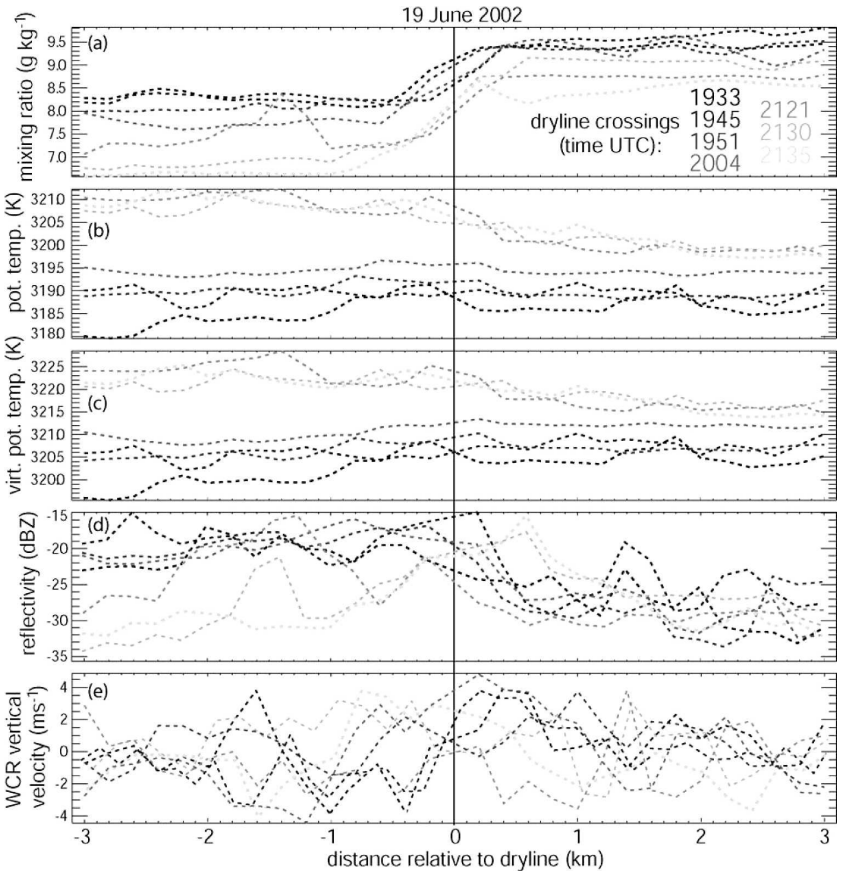

FIG. 9. Composite of WKA measurements across the 19 Jun dryline, illustrating temporal change. The lines become lighter with time. Flight levels range between 150 and 900 m AGL, all well within the CBL on both sides of the dryline. All data apply to flight level, except the WCR reflectivity and vertical velocity. These data are an average of the first seven range gates (210 m) from both the nadir and zenith antennas. (For the 150 m AGL flight legs, the first 14 gates from the zenith antenna are used.) All data have been averaged in along-track segments of 200 m.

tributed throughout the period, in particular the synoptic-scale wind shear associated with the decaying cold front and the west-bound ageostrophic acceleration toward the high plains where daytime surface heating caused surface pressure falls (Murphey et al. 2006). The acceleration of the moist-side southerly flow is quite apparent from the WKA data between 2004 to 2135 UTC (Fig. 8) and from several soundings (e.g., Fig. 7). Still, it is not clear how this leads to *finescale* convergence.

The largest $\Delta\theta_v$ value occurred in the last WKA flight leg and probably continued to increase afterward. An animation of the 0.5° elevation scan of the Goodland, Kansas, Weather Surveillance Radar-1988 Doppler (WSR-88D) radar shows that after 2135 UTC, the dryline accelerated toward the northwest. Thunderstorms erupted just east of the dryline and convective outflow may have enhanced the buoyancy deficit on the moist side and the westward propagation of the dryline, although thunderstorm outflows do not fully explain this retrogression, since the dryline also retrogressed in the gap region between thunderstorms.

4. Discussion

a. θ_v gradients across drylines, and finescale convergence

Several observational studies have documented a $\Delta\theta_v$ across the dryline, with values of about ~1.0 K (ranging between 0.5 and 1.9 K) over a distance of ~10 km (Table 2). The May 22 dryline $\Delta\theta_v$ is similar, but all others in this study have $\Delta\theta_v < 1.0$ K over 10 km (Table 1). The other drylines in this study also generally are weaker in terms of humidity contrast and confluence

TABLE 2. A comparison between (b) drylines and (a) other boundaries interpreted as density currents. Only observational studies are listed. The θ_v differences over distances of 10 and/or 25 km are estimated from published data or graphs. The lowest flight leg is used where aircraft data are available. Also listed are the following: in (a), the estimated density current depth D_{dc}; and in (b), the time or period of observations, h_{de}, and reported dryline motion. Negative values of dryline motion are westbound (retrogression).

(a) Nondryline boundaries interpreted as atmospheric density currents

Reference	Phenomenon	$\Delta\theta_v$ (K) over ~10 km	D_{dc} (km)
Geerts et al. (2006)	Cold front	4.1	0.8
Charba (1974)	Oklahoma gust front	6.1	1.3
Mueller and Carbone (1987)	Colorado gust front	4.3	1.2
Atkins and Wakimoto (1997)	6 Florida gust fronts	2.5	1.1
Kingsmill and Crook (2003)	10 Florida gust fronts	4.5	1.1
Atkins and Wakimoto (1997)	18 Florida sea-breeze fronts	1.1	0.5
Kingsmill and Crook (2003)	10 Florida sea-breeze fronts	2.0	0.7

(b) Drylines in west Texas/Oklahoma

Reference	Approx time (UTC)	$\Delta\theta_v$ (K) (estimated) 10-km scale	$\Delta\theta_v$ (K) (estimated) 25-km scale	h_{de} (km)	Dryline motion (m s^{-1})
Fig. 6 in NSSP Staff (1963)	2110	0.9	1.1	1.1	<0
Fig. 8 in Bluestein et al. (1990)	2230	1.5			
Fig. 8 in Parsons et al. (1991)	0100	—	1.9	1.2	−7.5
Fig. 8 in Ziegler and Hane (1993)	2110	1.8	2.1	1.3	<0
Fig. 5 in Hane et al. (1997)	2220	1.0	1.2	1.0	~0
Figs. 14 and 16 in Atkins et al. (1998); Fig. 12 in Ziegler and Rasmussen (1998); Fig. 1a (6 May 1995)	See Fig. 14	1.8	2–3	0.9	~0 to −1
Fig. 7 in Ziegler and Rasmussen (1998); Fig. 1b (7 Jun 1994)	See Fig. 14	1.9	2.0	1.5	~0
Fig. 2 in Ziegler and Rasmussen (1998) (15 May 1991)	1540–2330	0.5 early 1.5 late	1.0 early 3.0 late	0.6–1.2	+3 to 0

than the 22 May IHOP, the 6 May 1995 VORTEX, and the 7 June 1994 VORTEX drylines (Table 1) and, unlike these three cases, occurred under clear synoptic forcing and/or outside the main geographic area of drylines. In all cases listed in Table 2b, the moist air mass is the denser one. The 19 June case, with a reversal in the sign of $\Delta\theta_v$ and slope of the dryline updraft (SG07), is by no means a classic dryline.

Even in a boundary layer with vigorous convective motions, relatively small horizontal θ_v differences drive a solenoidal circulation in which the less-dense air (usually the dry air) rises over the denser air. The sharp humidity contrast found along the dryline (e.g., NSSP Staff 1963; Figs. 4, 8) is believed to be the direct result of the low-level confluence associated with the solenoidal circulation. This convergent circulation can be sustained as long as some meso-β θ_v gradient is present.

The null hypothesis of this study, that the presence and strength of convergence lines is independent of their air density contrast, can be rejected by the ensemble of boundaries analyzed herein. A clear correlation exists between Δu and $\Delta\theta_v$ (Table 1), although exceptions exist, in particular on 18 and 19 June. Baroclinic theory predicts confluence values similar to those observed, although this depends on the scale selected (Fig. 10). At larger scales the theory tends to yield an overestimate, but at all scales the linear regression slopes of predicted versus observed confluence, at matching scales, is close to 1:1, at least for the solenoidal confluence Eq. (6), where $|\Delta u| \propto \Delta\theta_{v,0}$ (Fig. 10). The predicted:observed Δu slope is smaller for the density current Eq. (9) at all scales (Fig. 10); that is, the confluence at weak (strong) θ_v boundaries is over- (under-) estimated. This suggests that the power in the proportionality, 0.5 [$|\Delta u| \propto \sqrt{\Delta\theta_{v,0}}$ in Eq. (9)], is too small.

The solenoidal forcing is believed to be the leading mechanism of linear, irregular (non-wave-like), finescale convergence over flat terrain. It should apply generally, not just in the geographic domain of drylines. Fine lines of often unclear origin are frequently found in the CBL during the warm season (e.g., Wilson and Schreiber 1986; Koch and Ray 1997). *Finescale conver-*

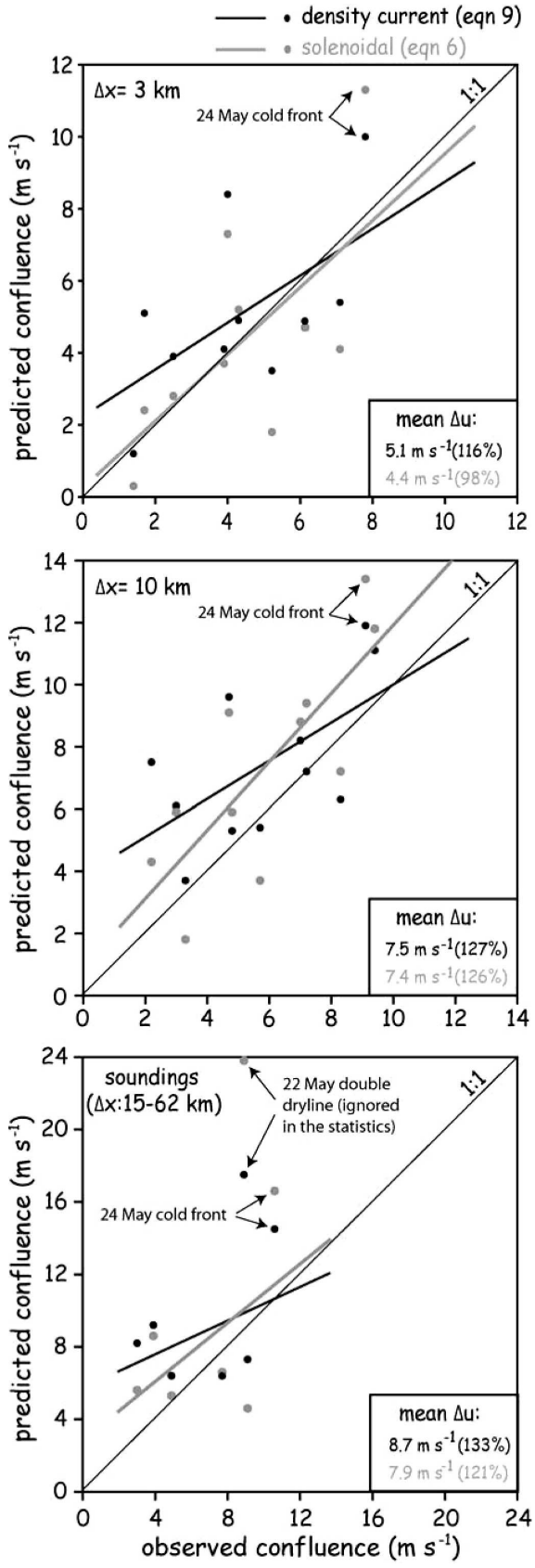

gence lines (drylines or other radar fine lines) are expected to form whenever the meso-β θ_v gradient (over Δx = 25 km or longer) exceeds some threshold. Our study suggests that this threshold is relatively small, <1.0 K $(25\ \text{km})^{-1}$ in some cases.

It is conceivable that on days with a large east–west gradient in daytime surface buoyancy flux over the southern/central Great Plains, this threshold is exceeded in several locations; thus several roughly parallel dryline boundaries may form in the afternoon, as observed in this study (on 22 May and 18 June) and elsewhere (e.g., Hane et al. 1997, 2002). Multiple fine lines are common in west Texas (C. Weiss 2006, personal communication). Closely spaced ancillary lines may coalesce into a single line, possibly by differential propagation related to differences in $\Delta\theta_v$, and the absorption of weaker boundaries by stronger ones (Kingsmill and Crook 2003).

b. *Differential CBL depth, westerly momentum transfer, and dryline formation*

The higher surface sensible heat flux west of the typical dryline formation zone results in a deeper CBL on the dry side, and this, in addition to the elevated topography to the west, allows westerly shear to produce convergence when westerly momentum is mixed vertically in the CBL (e.g., Hane et al. 1993). This process applies to the meso-β scale. It may also produce finescale convergence, especially in the presence of a CBL depth discontinuity (Hane et al. 1997).

The necessary conditions for this process are a deeper CBL on the west side ($h_{li} > h_{de}$) and "westerly" shear (or, more precisely, dryline-normal shear) in the h_{li} growth layer. The first condition is generally satisfied for the cases examined here, the second one is not, at least not for the cases for which suitable soundings are available. On 22 May 2002 strong westerly shear and momentum are present above the CBL top, but they did not increase between the two soundings; in fact, they weakened somewhat near h_{li} (Fig. 11a) during 2235 and 2329 UTC, a period during which $\Delta\theta_v$ across the primary dryline increased (section 3a, and section 4e

←

FIG. 10. Summary of boundary-normal confluence observations and predictions listed in Table 1. The black symbols apply to the density current Eq. (9), the gray ones to the solenoidal Eq. (6). Linear regression curves and mean values are shown in black and gray for the respective equations. The mean values are also expressed as a percentage of the observed mean, between brackets. (top) The 3-km averages, (middle) 10-km averages, and (bottom) values are derived from soundings.

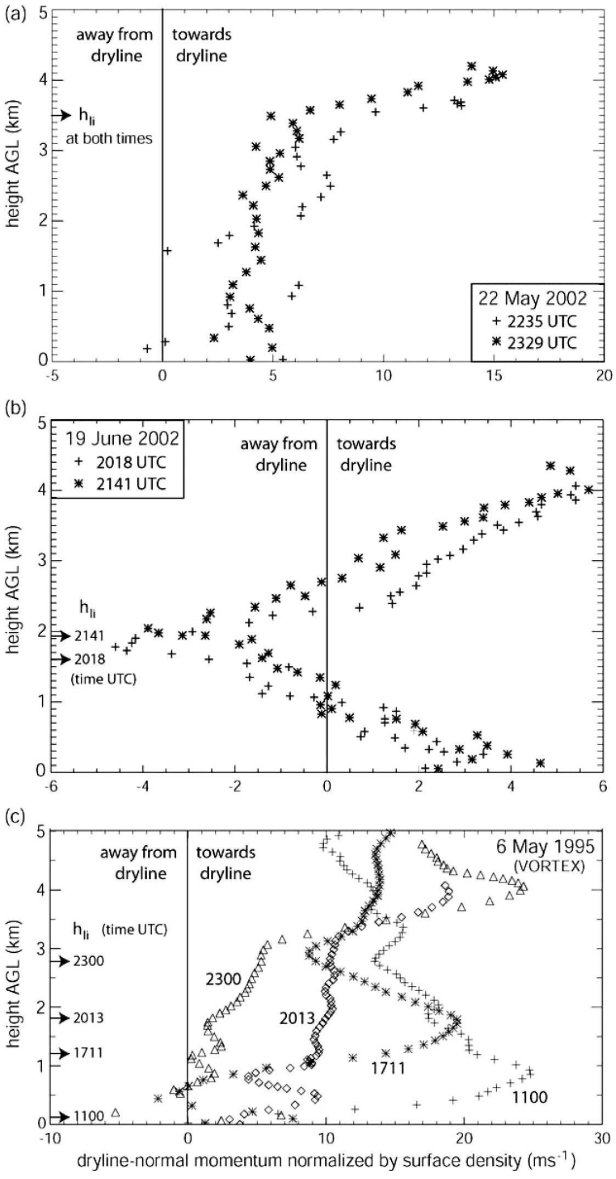

FIG. 11. Profiles of dryline-normal momentum on the dry side of the dryline at different times, on (a) 22 May 2002, (b) 19 Jun 2002, and (c) 6 May 1995, from soundings released at the times indicated, all within 30 km from the dryline.

below). Earlier, the dry-side CBL may have ingested westerly momentum from aloft as it deepened.

A more conclusive validation necessitates a time period of diurnal h_{li} increase: then at time 1 westerly shear is needed in the layer of CBL growth, and at time 2 increased westerly momentum is expected throughout the CBL. On 19 June 2002 (Fig. 11b) there is westerly shear above h_{li} in the early phase, but in the h_{li} growth layer, there is no westerly momentum on the dry side, and by the late phase, westerly momentum has not increased in the CBL. The strongest evidence that vertical momentum transfer in the deepening CBL does not drive momentum changes on the dry side of the developing dryline comes from the 6 May 1995 VORTEX case (Fig. 11c). Between 2013 and 2300 UTC, westerly momentum decreases, even though there is some westerly shear in the growth layer.

Even if differential vertical momentum transfer does occur, it may be a consequence of the development of a meso-γ $\Delta\theta_v$. The evidence presented here indicates that it is the latter that drives the circulation, the fine line, and the discontinuity in CBL depth.

c. *Solenoidal circulation and mixing in the dryline convergence zone*

Horizontal mixing does occur within the DCZ (e.g., Ziegler and Hane 1993; Atkins et al. 1998; Karan and Knupp 2006; Weiss et al. 2008), especially when the 10-km $\Delta\theta_v$ becomes large enough for a density current to develop with leading head and trailing turbulent wake. A first estimate of the DCZ width is given by the circulation around the density current head, about 2 km wide on 22 May (Fig. 5).

A clear circulation did not occur in the other, lower-$\Delta\theta_v$ cases in this study. Even on those days a circulation may have been present, but obscured by far stronger convective eddies. To extract evidence of a circulation, we examine the vertical profiles of the 3-km difference of WCR vertical velocity (Δw) and reflectivity (ΔZ) across the dryline (Fig. 12). The 3-km average is chosen to capture the solenoidal flow and reduce the convective "noise." Figure 12 only includes the "classical" drylines cases, with a denser moist side. Rising motion of the less dense air relative to the denser air implies negative Δw values (Fig. 12b). A tilt in the updraft plume toward the denser air would imply an increase in mean Δw with height. These features generally are observed on 22 May and on the three other days (Fig. 12b), although there is much scatter, and the difference from one flight leg to the next is large.

Inspired by the echo anvil spreading over the denser, moist air on 22 May (Figs. 2, 4) and over the cold postfrontal air on 24 May (Geerts et al. 2006), we examine the difference in reflectivity. Reflectivity may have more temporal continuity than vertical velocity, since it depends on some time integral of vertical motion (Geerts and Miao 2005). The solenoidal circulation implies near-zero ΔZ values near the surface and positive ΔZ in the middle and upper CBL, due to the spreading of the insect plume over the wedge of denser air. This is observed for 22 May, but in the other three cases the ΔZ profiles are widely scattered (Fig. 12a). This suggests that a clear secondary circulation is present only on 22 May, and that in general mixing in the DCZ is less

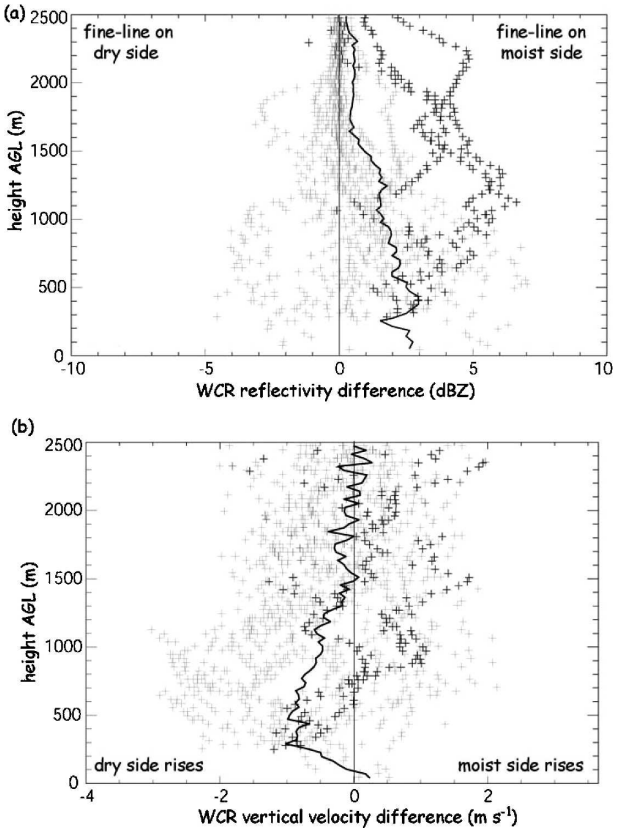

FIG. 12. Vertical variation of the difference in (a) WCR reflectivity and (b) WCR vertical velocity, across the dryline, on four days studied here. The difference is defined as (moist − dry) and is based on 3-km averages on either side of the dryline. Black symbols apply to the strong case (22 May), gray symbols to the other days. The solid line is the mean of all profiles. The profiles are based on seven flight legs on 22 May, and 16 legs on three other days, at various levels within the CBL. The early phase on 19 Jun, with reverse θ_v gradient, as well as the secondary drylines on 22 May and 18 Jun (Table 1), is excluded.

a result of a steady secondary circulation and more due to transient eddies (thermals) or horizontal variations (misocyclones).

The humidity trace generally shows a sharper discontinuity at the dryline than the θ_v trace, and θ_v is more likely than r to continue to decrease into the dense-air wedge, in the cases examined here (e.g., Fig. 4). These two characteristics have been documented in other dryline studies (NSSP Staff 1963; Parsons et al. 1991; Ziegler and Rasmussen 1998; Atkins et al. 1998; Karan and Knupp 2006). We believe that this is because the meso-β θ_v gradient is essential for the circulation to occur, while the meso-β humidity gradient, a common characteristic of dryline environments (e.g., Fig. 11 in Ziegler and Hane 1993), is more circumstantial. For all drylines listed in Table 1 (except the anomalous early phase on 19 June), and all scales, the potential temperature term (which makes the moist side more dense) is 2.8 times larger than the water vapor term (which makes the moist side less dense) in the expression for $\Delta\theta_v$. Thus to a first order water vapor can be regarded as a passive tracer.

d. A dryline as a density current

The typical $\Delta\theta_v$ is small across a dryline, compared to that across cold fronts and gust fronts (Table 2), yet often large enough for the dryline boundary to assume density current characteristics (e.g., Ziegler and Hane 1993; Atkins et al. 1998). The critical 10-km $\Delta\theta_v$ for density current characteristics to appear in a CBL may be close to 1.0 K, a value exceeded only on 22 May and the two VORTEX cases in Table 1. This value may depend on ambient shear. Florida sea breezes occur with an average $\Delta\theta_v$ of only 1.1 K and a shallow marine CBL (Atkins and Wakimoto 1997). A sea breeze was maybe the first atmospheric phenomenon to be compared to a laboratory density current (e.g., Clarke 1955). In many cases the dryline may well behave as an "inland sea breeze" (Sun and Ogura 1979; Sun 1987; Bluestein and Crawford 1997) at the meso-γ scale.

In principle a solenoidal circulation occurs over the depth of the θ_v difference, which varies between h_{de} and h_{li} (Figs. 1, 6). If $\Delta\theta_v$ is sufficient and sufficiently long lived for a density current to develop, its depth D_{dc} is not h, but rather a function of ambient shear normal to the dryline and h (Xue et al. 1997). For instance, the 24 May cold-frontal density current (Table 1) occupied only ~37% of the warm-side h. Published D_{dc} values vary widely (Table 2). Some studies report D_{dc} values less than h (Atkins and Wakimoto 1997) or even less than h_{de} (Atkins et al. 1998). The uncertainty in flow depth implies an uncertainty in the theoretical low-level confluence (Table 1). The fact that density current theory generally overestimates confluence (Fig. 10) may be due to an overestimate of D_{dc}. Another factor is that the feeder flow strength (8) probably is the maximum value in the rear-inflow current (Simpson et al. 1977), while WKA and sounding data represent averages.

Retrogression occurred in later stages in all cases studied here, except on 24 May, when a cold front moved in. In some cases, as on 19 June, changes in $\Delta\theta_v$ may explain or contribute to dryline retrogression. Dryline propagation is affected by the ambient low-level flow, which is variable and may be diurnally modulated. In most papers where the dryline has been characterized as a density current, retrogression is observed (Table 2), although Crawford and Bluestein (1997) report on retrogressing drylines without density current characteristics. Larger-scale factors contribute

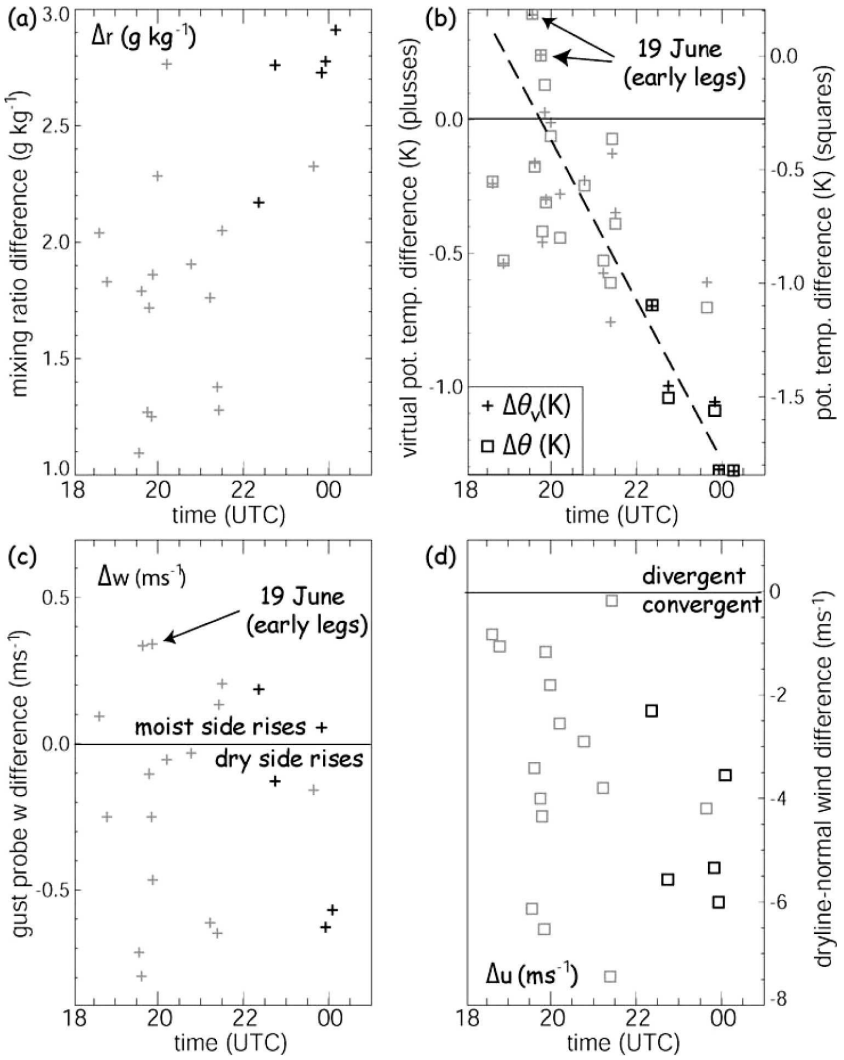

FIG. 13. Temporal change of the difference between moist and dry air, based on in situ WKA data at low flight levels (below $0.5h_{dc}$), for all dryline cases in this study (five legs on 22 May, three on 24 May, nine for 18 Jun, and four for 19 Jun). The difference (moist − dry) is based on 3-km averages, on opposite sides of the dryline moisture gradient. Black symbols apply to 22 May, gray symbols to the other days. The dashed line in (b) is the linear best fit for θ_v.

to this retrogression (e.g., Bluestein and Crawford 1997; Shaw et al. 1997), but on the scale of the density current, the hydrostatically higher surface pressure in the moist, cooler air drives ageostrophic flow westward, even if that direction locally is upslope (Mahrt 1982).

e. Diurnal dryline trend

It is remarkable that notwithstanding the clear synoptic "forcing" in all but one case in this study, and the range in geographic locales (from northwest Texas to northwest Kansas), a diurnal trend is apparent in the cross-dryline differences (Fig. 13). The humidity contrast does not change much, but $-\Delta\theta$ tends to increase with time toward 0000 UTC. The net result is that $-\Delta\theta_v$ tends to increase (Fig. 13b); this is consistent with an increase in low-level confluence, although such a trend is not clearly present (Fig. 13d). At a scale of 3 km, the gust probe data do not reveal a trend toward dry air rising over the moist air (Fig. 13c).

A similar trend emerges from previous dryline studies (Table 2b), although detailed data are often missing. The 7 June 1994 (Ziegler and Rasmussen 1998) and 6 May 1995 (Atkins et al. 1998; Ziegler and Rasmussen 1998) dryline case studies appear to be among the best available. In these studies flight-level water vapor was measured by a chilled-mirror dewpoint sensor on the

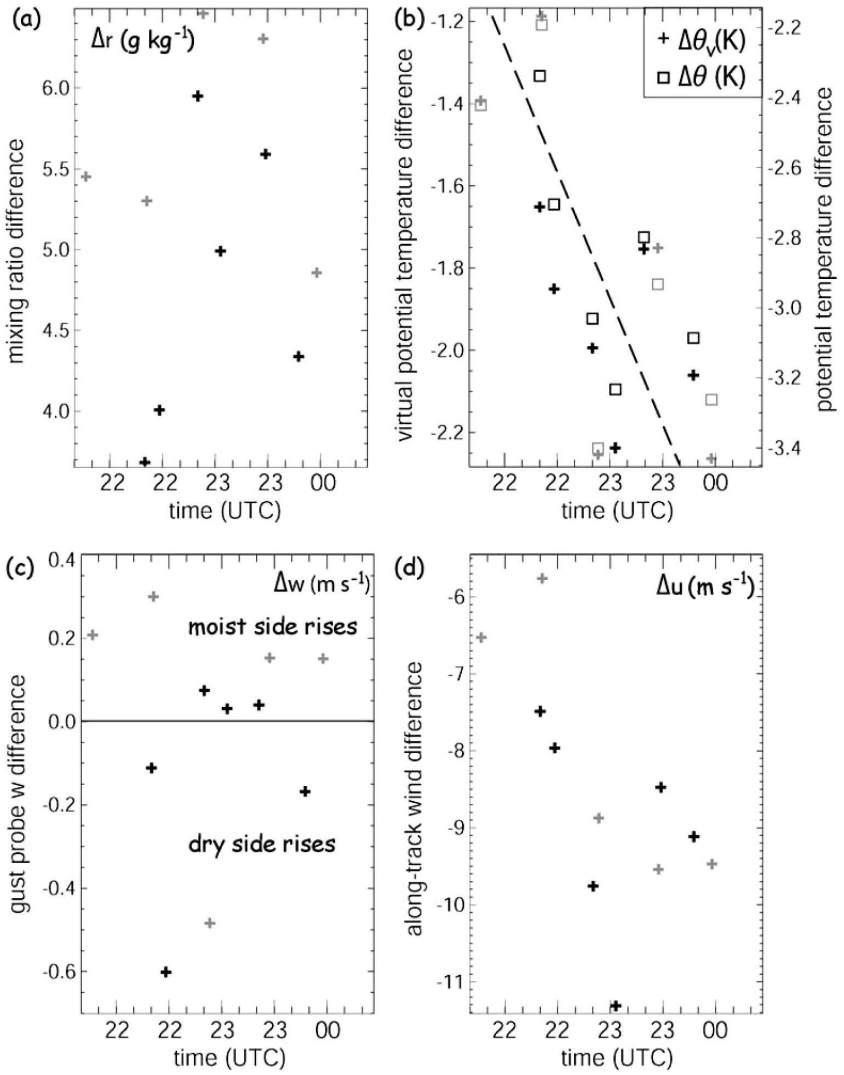

FIG. 14. As in Fig. 13, but based on 10-km averages, for six dryline crossings below 600 m AGL on 7 Jun 1994 (black symbols) and five dryline crossings at ~180 m AGL on 6 May 1995 (gray symbols). The data were collected by the NOAA P-3 during VORTEX.

National Oceanic and Atmospheric Administration (NOAA) P-3 aircraft. This is a slow-response sensor; thus it displayed a hysteresis when the aircraft encountered a sharp moisture gradient (Ziegler and Hane 1993). Overshooting (undershooting) occurs when the probe experiences a sudden humidity increase (decrease). Overshoots (undershoots) often appear as sharp spikes (exponential decays) in the time series of r. The width of the spikes varies from 10 to 20 s, and the exponential adjustment can take 30 s (~3.3 km along-track). For this reason, no reliable 3-km averages can be taken. One cannot accurately correct bad data, so we removed them. For overshoots, we determined the first and last stable values at each side of the spikes. For undershoots, we eliminated 30 s of data from the last trustable point at the moist side. Averages of any variable were then computed from the 1-Hz NOAA P-3 data over 10 km from either side of the best-guess dryline location, excluding the flagged times.

The resulting differences for the two VORTEX cases (Fig. 14) are generally larger than the 3-km differences for the IHOP drylines (Fig. 13). The 10-km Δr, $\Delta\theta_v$, and Δu values (~5.2 g kg^{-1}, ~1.9 K, and ~8.3 m s^{-1} respectively) are significantly larger than on 22 May 2002 (Table 1). But the diurnal trends of Δr, $\Delta\theta$, and $\Delta\theta_v$ are similar. Dryline-normal confluence Δu tends to increase as well, consistent with the $\Delta\theta_v$ trend (Fig. 14d). Notwithstanding the larger $\Delta\theta_v$, there is still no evidence for ascent of dry air over moist air at a scale of 10 km (Fig. 14c).

The diurnal trend of $\Delta\theta_v$ in both IHOP and VORTEX drylines suggests that $\Delta\theta_v$ is largely driven by regional differences in surface heat fluxes, which are strongly diurnally modulated. The difference in surface buoyancy fluxes probably peaks before 0000 UTC (~5 h 20 min after local solar noon), but the sign of the difference may be maintained until at least 0000 UTC. The regional θ_v gradient then increases at finer scales by baroclinic circulations. Thus dryline characteristics probably are strongly affected by regional differences in surface heat fluxes. We hope to examine this further in a future campaign that includes regional flux estimates.

5. Conclusions

The finescale kinematic and thermodynamic properties of several radar fine lines observed in IHOP are examined. All boundaries are marked by a sharp humidity contrast; therefore they are referred to as drylines. Significant along-line horizontal variability exists in some cases, but the focus of this study is on the vertical structure. The main conclusions are as follows:

- All fine lines are convergent and the convergence strength generally is related to their meso-γ-scale air density contrast, expressed in terms of $\Delta\theta_v$.
- Two methods, one based on a steady solenoidal circulation and the other on density current theory, are used to estimate the meso-γ-scale convergence Δu near a baroclinic boundary. The solenoidal confluence is proportional the CBL depth and $\Delta\theta_v$, while the density current confluence is proportional to their square root. The former yields a slope of predicted versus observed confluence close to 1:1 for the cases examined here. Both methods tend to overestimate confluence, especially for well-defined boundaries (large $\Delta\theta_v$). The optimal scale at which $\Delta\theta_v$ and Δu are measured appears relatively small: both methods tend to overestimate Δu more when $\Delta\theta_v$ is computed at distances Δx of 10 km or more.
- One boundary, the 22 May primary dryline, has a clearly sloping reflectivity and updraft plume, a rear-inflow current, a secondary circulation in the vertical plane across the dryline, and other density current characteristics. The moist air mass is denser, with a $\Delta\theta_v$ of 1.3 K over 10 km, decreasing with height in the CBL.
- Other fine lines, observed outside the classic domain of dryline occurrence and/or under synoptically disturbed conditions, are all are marked by some low-level $\Delta\theta_v$, but less than 1.0 K over 10 km. Some slope in the echo plume, toward the denser air mass, is generally present, but WCR data reveal no solenoidal circulation. Thus, especially in weak $\Delta\theta_v$ cases, mixing in the DCZ appears to be dominated by convective activity and possible along-line variability, not a secondary circulation. Sometimes the finescale confluence exceeds that expected from baroclinicity alone, in particular in the late phases of 18 and 19 June, during convective initiation.
- In most cases a meso-β-scale θ_v gradient is present. A threshold gradient may exist for the development of one or more radar fine lines, concentrating the $\Delta\theta_v$. Limited observations herein suggest that this threshold is rather low, 1.0 K $(25\ \text{km})^{-1}$ or even less. Similarly, fine-line boundaries may assume density-current properties once their $\Delta\theta_v$ exceeds a threshold, about 1.0 K over 10 km.
- This study does not lend credence to the idea that differential vertical transfer of boundary-normal momentum, associated with differences in CBL depth across a dryline, produces finescale convergence.
- This study reveals an unexpected diurnal trend of the meso-γ-scale $\Delta\theta_v$ across drylines in both IHOP and VORTEX. We speculate but do not demonstrate that this results from a diurnally varying meso-β-scale $\Delta\theta_v$ that is largely driven by differential surface heat fluxes.

Acknowledgments. The National Science Foundation, Grant ATMS0129374, supported this research. Sam Haimov was responsible for the WCR data collection. Rick Damiani developed the WCR Doppler velocity analysis package. Conrad Ziegler provided the NOAA P-3 data for 7 June 1994 and 6 May 1995 and advised us on the use of the data. Margaret LeMone reviewed an early draft of the document.

REFERENCES

Arnott, N. R., Y. P. Richardson, J. M. Wurman, and E. M. Rasmussen, 2006: Relationship between a weakening cold front, misocyclones, and cloud development on 10 June 2002 during IHOP. *Mon. Wea. Rev.,* **134,** 311–335.

Atkins, N. T., and R. M. Wakimoto, 1997: Influence of the synoptic-scale flow on sea breezes observed during CaPE. *Mon. Wea. Rev.,* **125,** 2112–2130.

——, ——, and C. L. Ziegler, 1998: Observations of the finescale structure of a dryline during VORTEX 95. *Mon. Wea. Rev.,* **126,** 525–550.

Bjerknes, V., 1898: Über einen hydrodynamischen Fundamentalsatz und seine Anwendung besonders auf die Mechanik der Atmosphäre und des Weltmeeres. *Kongl. Sven. Vetensk. Akad. Handlingar,* **31,** 1–35.

Bluestein, H. B., and T. M. Crawford, 1997: Mesoscale dynamics of the near-dryline environment: Analysis of data from COPS-91. *Mon. Wea. Rev.,* **125,** 2161–2175.

——, E. W. McCaul Jr., G. P. Byrd, R. L. Walko, and R. Davies-

Jones, 1990: An observational study of splitting convective clouds. *Mon. Wea. Rev.,* **118,** 1359–1370.

Charba, J., 1974: Application of gravity current model to analysis of squall-line gust front. *Mon. Wea. Rev.,* **102,** 140–156.

Clarke, R. H., 1955: Some observations and comments on the sea breeze. *Aust. Meteor. Mag.,* **11,** 47–68.

Crawford, T. M., and H. B. Bluestein, 1997: Characteristics of dryline passage during COPS-91. *Mon. Wea. Rev.,* **125,** 463–477.

Damiani, R., and S. Haimov, 2006: A high-resolution dual-Doppler technique for fixed multi-antenna airborne radar. *IEEE Trans. Geosci. Remote Sens.,* **44,** 3475–3489.

Demoz, B., and Coauthors, 2006: The dryline on 22 May 2002 during IHOP_2002: Convective-scale measurements at the profiling site. *Mon. Wea. Rev.,* **134,** 294–310.

Doswell, C. A., III, and P. M. Markowski, 2004: Is buoyancy a relative quantity? *Mon. Wea. Rev.,* **132,** 853–863.

Geerts, B., and Q. Miao, 2005: The use of millimeter Doppler radar echoes to estimate vertical air velocities in the fair-weather convective boundary layer. *J. Atmos. Oceanic Technol.,* **22,** 225–246.

——, R. Damiani, and S. Haimov, 2006: Fine-scale vertical structure of a cold front as revealed by airborne radar. *Mon. Wea. Rev.,* **134,** 251–272.

Grossman, R. L., D. Yates, M. A. LeMone, M. L. Wesely, and J. Song, 2005: Observed effects of horizontal radiative surface temperature variations on the atmosphere over a Midwest watershed during CASES 97. *J. Geophys. Res.,* **110,** D06117, doi:10.1029/2004JD004542.

Hane, C. E., C. L. Ziegler, and H. B. Bluestein, 1993: Investigation of the dryline and convective storms initiated along the dryline: Field experiments during COPS-91. *Bull. Amer. Meteor. Soc.,* **74,** 2133–2145.

——, H. B. Bluestein, T. M. Crawford, M. E. Baldwin, and R. M. Rabin, 1997: Severe thunderstorm development in relation to along-dryline variability: A case study. *Mon. Wea. Rev.,* **125,** 231–251.

——, R. M. Rabin, T. M. Crawford, H. B. Bluestein, and M. E. Baldwin, 2002: A case study of severe storm development along a dryline within a synoptically active environment. Part II: Multiple boundaries and convective initiation. *Mon. Wea. Rev.,* **130,** 900–920.

Houze, R. A., 1993: *Cloud Dynamics*. Academic Press, 573 pp.

Jin, Y., S. E. Koch, Y.-L. Lin, M. F. Ralph, and C. Chen, 1996: Numerical simulations of an observed gravity current and gravity waves in an environment characterized by complex stratification and shear. *J. Atmos. Sci.,* **53,** 3570–3588.

Jones, P. A., and P. R. Bannon, 2002: A mixed-layer model of the diurnal dryline. *J. Atmos. Sci.,* **59,** 2582–2593.

Kaimal, J. C., J. C. Wyngaard, D. A. Haugen, O. R. Cote, Y. Izumi, S. J. Caughey, and C. J. Readings, 1976: Turbulence structure in the convective boundary layer. *J. Atmos. Sci.,* **33,** 2152–2169.

Karan, H., and K. Knupp, 2006: Mobile Integrated Profiler System (MIPS) observations of low-level convergent boundaries during IHOP. *Mon. Wea. Rev.,* **134,** 92–112.

Kingsmill, D. E., and N. A. Crook, 2003: An observational study of atmospheric bore formation from colliding density currents. *Mon. Wea. Rev.,* **131,** 2985–3002.

Koch, S. E., and C. A. Ray, 1997: Mesoanalysis of summertime convergence zones in central and eastern North Carolina. *Wea. Forecasting,* **12,** 56–77.

Liu, C., and M. W. Moncrieff, 1996: A numerical study of the effects of ambient flow and shear on density currents. *Mon. Wea. Rev.,* **124,** 2282–2303.

Mahrt, L., 1982: Momentum balance of gravity flows. *J. Atmos. Sci.,* **39,** 2701–2711.

Markowski, P., and C. Hannon, 2006: Multiple-Doppler radar observations of the evolution of vorticity extrema in a convective boundary layer. *Mon. Wea. Rev.,* **134,** 355–374.

Marquis, J. N., Y. P. Richardson, and J. M. Wurman, 2007: Kinematic observations of misocyclones along boundaries during IHOP. *Mon. Wea. Rev.,* **135,** 1749–1768.

Miao, Q., 2006: Fine-scale vertical structure of clear-air echoes as detected by an airborne Doppler radar during the International H_2O Project. Ph.D. dissertation, University of Wyoming, 222 pp.

——, B. Geerts, and M. LeMone, 2006: Vertical velocity and buoyancy characteristics of echo plumes in the convective boundary layer, detected by a profiling airborne radar. *J. Appl. Meteor. Climatol.,* **45,** 838–855.

Miles, J. W., and L. N. Howard, 1964: Note on a heterogeneous shear flow. *J. Fluid Mech.,* **20,** 331–336.

Mueller, C. K., and R. E. Carbone, 1987: Dynamics of a thunderstorm outflow. *J. Atmos. Sci.,* **44,** 1879–1898.

Murphey, H. V., R. M. Wakimoto, C. Flamant, and D. E. Kingsmill, 2006: Dryline on 19 June 2002 during IHOP. Part I: Airborne Doppler and LEANDRE II analyses of the thin line structure and convection initiation. *Mon. Wea. Rev.,* **134,** 406–430.

NSSP Staff, 1963: Environmental and thunderstorm structures as shown by National Severe Storms Project observations in spring 1960 and 1961. *Mon. Wea. Rev.,* **91,** 271–292.

Parsons, D. B., M. A. Shapiro, M. R. Hardesty, R. J. Zamora, and J. M. Intrieri, 1991: The finescale structure of a west Texas dryline. *Mon. Wea. Rev.,* **119,** 1242–1258.

Rotunno, R., J. B. Klemp, and M. L. Weisman, 1988: A theory for strong, long-lived squall lines. *J. Atmos. Sci.,* **45,** 463–485.

Schaefer, J. T., 1974: The life cycle of the dryline. *J. Appl. Meteor.,* **13,** 444–449.

Shaw, B. L., R. A. Pielke, and C. L. Ziegler, 1997: A three-dimensional numerical simulation of a Great Plains dryline. *Mon. Wea. Rev.,* **125,** 1489–1506.

Simpson, J. E., and R. E. Britter, 1980: A laboratory model of an atmospheric mesofront. *Quart. J. Roy. Meteor. Soc.,* **106,** 485–500.

——, D. A. Mansfield, and J. R. Milford, 1977: Inland penetration of sea-breeze fronts. *Quart. J. Roy. Meteor. Soc.,* **103,** 47–76.

Sipprell, B. D., and B. Geerts, 2007: Finescale vertical structure and evolution of a preconvective dryline on 19 June 2002. *Mon. Wea. Rev.*, **35,** 2111–2134.

Smith, R. K., and M. J. Reeder, 1988: On the movement and low-level structure of cold fronts. *Mon. Wea. Rev.,* **116,** 1927–1944.

Stull, R. B., 1988: *An Introduction to Boundary Layer Meteorology*. Kluwer Academic, 666 pp.

Sun, W.-Y., 1987: Mesoscale convection along the dryline. *J. Atmos. Sci.,* **44,** 1394–1403.

——, and Y. Ogura, 1979: Boundary layer forcing as a possible trigger to squall line formation. *J. Atmos. Sci.,* **36,** 235–254.

——, and C.-C. Wu, 1992: Formation and diurnal variation of the dryline. *J. Atmos. Sci.,* **49,** 1606–1619.

Wakimoto, R. M., 1982: The life cycle of thunderstorm gust fronts as viewed with Doppler radar and rawinsonde data. *Mon. Wea. Rev.,* **110,** 1060–1082.

——, and B. L. Bosart, 2000: Airborne radar observations of a cold front during FASTEX. *Mon. Wea. Rev.,* **128,** 2447–2470.

Weckwerth, T. M., and R. M. Wakimoto, 1992: The initiation and organization of convective cells atop a cold-air outflow boundary. *Mon. Wea. Rev.,* **120,** 2169–2187.

——, and Coauthors, 2004: An overview of the International H_2O Project (IHOP_2002) and some preliminary highlights. *Bull. Amer. Meteor. Soc.,* **85,** 253–277.

Weiss, C. C., H. B. Bluestein, and A. L. Pazmany, 2006a: Finescale radar observations of the 22 May 2002 dryline during the International H2O Project (IHOP). *Mon. Wea. Rev.,* **134,** 273–293.

——, ——, ——, and B. Geerts, 2008: Finescale radar observations of a dryline during the International H2O Project (IHOP_2002). *Sanders Symposium Monograph, Meteor. Monogr.,* No. 55, Amer. Meteor. Soc., in press.

Wilson, J. W., and W. E. Schreiber, 1986: Initiation of convective storms by radar-observed boundary-layer convergent lines. *Mon. Wea. Rev.,* **114,** 2516–2536.

——, and D. L. Megenhardt, 1997: Thunderstorm initiation, organization, and lifetime associated with Florida boundary layer convergence lines. *Mon. Wea. Rev.,* **125,** 1507–1525.

——, and R. D. Roberts, 2006: Summary of convective storm initiation and evolution during IHOP: Observational and modeling perspective. *Mon. Wea. Rev.,* **134,** 23–47.

——, G. B. Foote, N. A. Crook, J. C. Fankhauser, C. G. Wade, J. D. Tuttle, and C. K. Mueller, 1992: The role of boundary layer convergence zones and horizontal rolls in the initiation of thunderstorms: A case study. *Mon. Wea. Rev.,* **120,** 1785–1815.

——, T. M. Weckwerth, J. Vivekanandan, R. M. Wakimoto, and R. W. Russell, 1994: Boundary-layer clear-air radar echoes: Origin of echoes and accuracy of derived winds. *J. Atmos. Oceanic Technol.,* **11,** 1184–1206.

Xue, M., and W. J. Martin, 2006: A high-resolution modeling study of the 24 May 2002 dryline case during IHOP. Part I: Numerical simulation and general evolution of the dryline and convection. *Mon. Wea. Rev.,* **134,** 149–171.

——, Q. Xu, and K. K. Droegemeier, 1997: A theoretical and numerical study of density currents in nonconstant shear flows. *J. Atmos. Sci.,* **54,** 1998–2019.

Ziegler, C. L., and C. E. Hane, 1993: An observational study of the dryline. *Mon. Wea. Rev.,* **121,** 1134–1151.

——, and E. N. Rasmussen, 1998: The initiation of moist convection at the dryline: Forecasting issues from a case study perspective. *Wea. Forecasting,* **13,** 1106–1131.